Spring 4-27-2023

Solar Sailing Adaptive Control Using Integral Concurrent Learning for Solar Flux Estimation

Luis Mendoza Zambrano
mendol10@my.erau.edu

By

A Thesis Submitted to the Faculty of Embry-Riddle Aeronautical University

In Partial Fulfillment of the Requirements for the Degree of

Master of Science in Aerospace Engineering

Embry-Riddle Aeronautical University

Daytona Beach, Florida

By

THESIS COMMITTEE

Graduate Program Coordinator, Dr. Hever Moncayo	Date
Dean of the College of Engineering, Dr. James W. Gregory	Date
Associate Provost of Academic Support, Dr. Christopher Grant	Date

To my family, for their unconditional love, support, and encouragement.

ACKNOWLEDGMENTS

First and foremost, I would like to thank my advisor, Dr. Riccardo Bevilacqua, for his guidance during my academic career. Thank you for placing your trust and confidence in my abilities. I would also like to express my gratitude to the committee members, Dr. Morad Nazari and Dr. Richard Prazenica, for taking the time to support and assess the presented work. I sincerely appreciate the provided feedback and tutelage during my first year in graduate school at Embry-Riddle. I would also like to thank you for the respect and values portrayed in our memorable talks and meetings. It was an honor and privilege to work with you. I am glad the journey has just started. I am grateful for being part of the Embry-Riddle community.

I would like to thank my family for their unconditional love, support, and encouragement. Especially, I would like to present in writing my deep affection to my parents and brother for their sacrifice and care throughout my entire life. Without your support and life lessons, this would not have been possible.

ABSTRACT

In the interest of exploiting natural forces for propellant-less spacecraft missions, this thesis proposes an adaptive control strategy to account for unknown parameters in the dynamic modeling of a reflectivity-controlled solar sail spacecraft. A Lyapunov-based control law along with integral concurrent learning is suggested to accomplish and prove global exponential tracking of the estimated parameters and states of interest, without satisfying the common persistence of excitation condition, which in most nonlinear systems cannot be guaranteed a priori. This involves estimating the solar flux or irradiance from the Sun to account for uncertainty and variation over time in this value. To illustrate potential applications, two missions are considered: (1) a geostationary debris removal case and (2) an Earth-Mars interplanetary transfer orbit following a logarithmic spiral reference trajectory. The proposed formulation demonstrates the benefit of estimating the solar flux using integral concurrent learning. Results are compared to trajectories with no estimation to illustrate the need to account for solar flux fluctuations. For near-Earth maneuvers, the steady state estimation error is recorded as 0.33 W/m^2. Similarly, the mean error for an Earth-Mars transfer is reported as 0.38 W/m^2, or equivalently 0.03%. This clearly indicates that the suggested adaptive control law used to estimate the solar flux accurately approximates its actual value.

TABLE OF CONTENTS

LIST OF FIGURES

LIST OF TABLES

Table **Page**

NOMENCLATURE

$\hat{\boldsymbol{n}}$	Sail's Surface Unit Normal Vector
$\boldsymbol{\theta}$	Uncertain Parameters
$\boldsymbol{a}_d$	Acceleration due to Orbital Perturbations
$\boldsymbol{a}_{\leftmoon}$	Acceleration due to the Moon's Gravity
$\boldsymbol{a}_{\odot}$	Acceleration due to the Sun's Gravity
$\boldsymbol{a}_{srp}$	Acceleration due to Solar Radiation Pressure
$\boldsymbol{e}$	Tracking Error
$\boldsymbol{P}$	Total Disturbance Acceleration
$\boldsymbol{q_m}$	Modified Equinoctial Orbital Element Set
$\boldsymbol{q}$	Classical Orbital Element Set
$\boldsymbol{r}$	Spacecraft's Position Vector
$\boldsymbol{r}_{\leftmoon/C}$	Moon's Position Vector Relative to Spacecraft
$\boldsymbol{r}_{\leftmoon}$	Moon's Position Vector
$\boldsymbol{r}_{\odot/C}$	Sun's Position Vector Relative to Spacecraft
$\boldsymbol{r}_{\odot}$	Sun's Position Vector
$\boldsymbol{u}$	System's Input
$\boldsymbol{v}$	Spacecraft Velocity Vector
$\boldsymbol{x}$	System's States

$\boldsymbol{x}_d$	Desired States
$\ddot{\boldsymbol{r}}$	Spacecraft's Acceleration Vector
$\Delta\boldsymbol{\theta}$	Estimation Error
ϵ	Film Emissivity
Γ	Tunning Gain Matrix
γ	Tunning Control Gain
$\hat{\boldsymbol{\theta}}$	Estimated Parameters
$\hat{\boldsymbol{e}}_{\odot}$	Sun's Position Unit Vector
$\hat{\boldsymbol{r}}$	In-Track Direction
$\hat{\boldsymbol{s}}$	Cross-Track Direction
$\hat{\boldsymbol{w}}$	Normal Direction
$\hat{P}_{srp}$	Estimated SRP Coefficient
λ	Eigenvalues
μ	Gravitational Parameter of Primary Body
$\mu_{\oplus}$	Earth's Gravitational Parameters
$\mu_{\leftmoon}$	Moon's Gravitational Parameter
$\mu_{\odot}$	Sun's Gravitational Parameter
Ω	Orbit's Right Ascension of the Ascending Node
ω	Orbit's Argument of Periapsis
ϕ_{inc}	Sail's Incidence Angle

σ	Spectrum of Eigenvalues
τ	Integration Variable
AU	Astronomical Unit
$\tilde{r}$	Reflection Coefficient
A	State Matrix
a	Orbit's Semi-Major Axis
A_s	Aluminized Film Area
A_{RCD}^{on}	Area Covered by Switched-On RCDs
A_{tot}	Total Exposed Area to Sunlight
B	Non-Lambertian Coefficient
b_i	Dimensionless Force Coefficients for $i = \{1, 2, 3\}$
c	Speed of Light
$C_{2,0}$	Second Zonal Harmonic Coefficient
$C_{2,2}$	Second Tesseral Harmonic Coefficient
d	Number of Days Since December 1^{st} of 2019
e	Orbit's Eccentricity
f	Reflectivity Modulation Ratio
h	Orbit's Angular Momentum Magnitude
I	Identity Matrix
i	Orbit's Inclination

K	State Feedback Gain Matrix
K_{ICL}	Integral Concurrent Learning Control Gain Matrix
L	True Longitude
m	Spacecraft's Mass
n	Orbit's Mean Motion
p	Orbit's Semi-Latus Rectum
P_{srp}	Solar Radiation Pressure Coefficient
Q	Transformation Matrix
$R_{\oplus}$	Earth's Mean Radius
$r_{\odot}$	Spacecraft's Distance to the Sun
s	Fraction of Photons Specularly Reflected
T	Final Time
t	Time Variable
u	Orbit's Argument of Latitude
V	Conical Shadow Coefficient
V	Lyapunov Candidate
W	Solar Flux
Y	Regression Matrix

1 Introduction

In the interest of exploiting natural forces for propellant-less spacecraft missions, numerous solar sail missions are proposed for a wide variety of applications including space exploration, relay communication, technology demonstration missions, *etc* [3]. For instance, NASA's Near-Earth Asteroid (NEA) Scout Mission, recently onboarded the Space Launch System (SLS), will help determine the physical properties of a near-Earth asteroid using a science-grade camera. The NEA Scout is a CubeSat propelled by a solar sail measuring 925 square feet [4]. In parallel, NASA is developing a new deployable structure known as Advanced Composite Solar Sail System, or *ACS3*, to demonstrate successful sail packing and deployment of composite solar sails within low-Earth orbits (Figure 1.1) [1]. NASA is also conducting research in diffractive lightsails proposed as a new solar sail concept that would use small gratings embedded in thin films to make a more efficient use of sunlight without sacrificing maneuverability [5]. However, for many solar sail mission applications, active control is required for the stability of a desired orbit. For a solar sail of fixed geometry and characteristic acceleration, active control is unattainable as the only control variables are given by the sail's attitude [6–8]. In this context, two proposed solutions to this problem are considered in the literature among which solar flux fluctuations are often neglected. One assumes a variable-geometry solar sail model [9], while the second one suggests the implementation of reflectivity modulation technology for orbital control.

1.1 Background

Reflectivity modulation technology is adopted for active control of solar sails in accordance with previous demonstration missions and applications [2, 6, 7]. A reflectivity control device (RCD) is a device manufactured from electrochromic materials composed of a thin layer of liquid crystals [10]. Effectively, upon application of a low electric voltage, crystals within the film align with the electric field, allowing its reflectivity coefficient to change from a diffusive to a highly specular state [10]. IKAROS (2010), the world's first successful interplanetary solar sail demonstration mission, used RCDs for attitude control [2].

Recent research on orbital control of solar sails using RCDs assumes real-time measurements of the solar flux are available [8]. Alternatively, in most academic papers, solar flux fluctuations are often neglected owing to the assumption of a constant solar radiation pressure coefficient. In addition, it is commonly assumed to be a known parameter. However, motivated by the desire to increase robustness and improve transient performance, as well as to avoid the implementation of a solar flux measuring device that would only increase the mission cost and compromise control capabilities, adaptive control along with concurrent learning (CL) is used to estimate and account for uncertainties and variation over time in unknown parameters without satisfying the common persistence of excitation (PE) condition, which for nonlinear systems cannot be guaranteed a priori and is difficult to check online [11]. More precisely, integral concurrent learning (ICL) is suggested as a modified CL formulation with better tracking and estimation performance in which estimation of the states derivatives is not required [12].

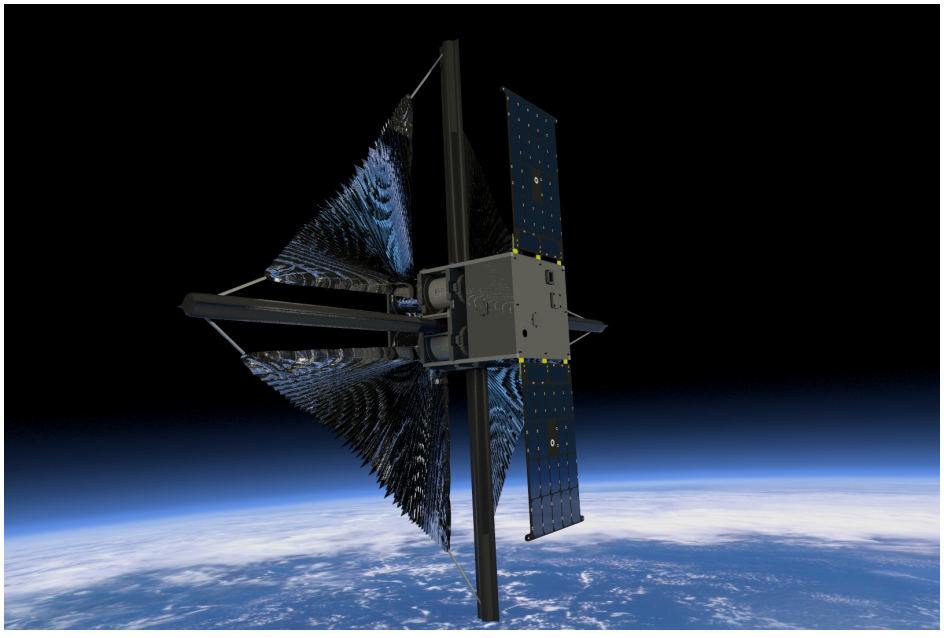

Figure 1.1 Advanced Composite Solar Sail System *ACS3* concept by NASA [1].

As recent studies have shown the need to account for solar flux fluctuations [13, 14], this thesis proposes an adaptive control strategy to account for unknown parameters in the dynamic modeling of a reflectivity-controlled solar sail spacecraft. This requires determining the spacecraft's orientation to achieve a desired maneuver within realistic time compared to optimal control schemes found in the literature [8, 15]. A Lyapunov-based control law along with integral concurrent learning is suggested to accomplish and prove global exponential tracking of the estimated parameters and states of interest, without satisfying the persistence of excitation condition. This involves estimating the solar flux or irradiance from the Sun to account for uncertainty and variation over time in this value.

1.2 Problem Statement

Since 1978, absolute radiometers have been onboarded satellites to measure the solar flux for solar-observation studies [16]. However, as noted in recent literature, there is no consensus on a single total solar irradiance (TSI) time series as different radiometers measure inconsistent values. In addition, the long-term TSI variability has not been established as most radiometers do not exceed more than a decade due to material degradation [16]. As a result, the solar flux variation due to the 11-year solar cycle has not been accurately characterized. Indeed, accurate solar flux measurements represent a current challenge in the scientific community. The Compact Total Irradiance Monitor-Flight Demonstration (CTIM-FD) mission by NASA is one of the many solar-observation missions in progress that aim to study solar flux variability. The CTIM-FD mission is currently testing future technology for TSI measurements [17]. In this sense, a solar flux measurement package part of the attitude and orbital control system, as proposed in the literature to account for solar flux fluctuations, would not be ideal. Alternatively, we suggest an adaptive control scheme along with integral concurrent learning to estimate the irradiance from the Sun.

1.3 Objectives

Unlike preliminary research in solar sailing, this thesis presents an integral concurrent learning approach to estimate the solar flux as opposed to assuming real-time measurements are available. This thesis aims to prove global exponential tracking of the estimated parameters and states of interest. To illustrate potential applications, two missions are considered: (1) a geostationary debris removal case and (2) an Earth-Mars interplanetary transfer orbit following a logarithmic spiral reference trajectory. Results are compared to trajectories with no estimation to illustrate the need to account for solar flux fluctuations.

1.4 Contributions

Within the objectives of this thesis, a summary of the contributions is outlined as follows:

- We present a method to estimate the solar flux using integral concurrent learning.
- To the author's knowledge, this is the first attempt within academia in estimating the solar flux using measurable input-to-output data corresponding to the spacecraft's state vector.
- A gradient-based control law for the sail's orientation using Gauss' variational equations (GVEs) is developed to guarantee asymptotic stability for near-Earth maneuvers.
- Results are compared to trajectories with no estimation to illustrate the need to account for solar flux fluctuations.

1.5 Thesis Outline

In Chapter 1, introductory background on reflectivity modulation technology for active control of solar sails is presented. Adaptive control along with integral concurrent learning is suggested to estimate the irradiance from the Sun to account for uncertainty and variation over time in this value. The problem statement is discussed in great detail followed by a brief summary of the objectives and contributions of this thesis.

In Chapter 2, an extensive literature review on the total solar irradiance effects on low-eccentricity and interplanetary orbits is discussed. Similarly, the state of the art in solar sailing guidance, navigation, and control as well as current challenges in solar-observation studies are presented. In addition, a review of adaptive control using Lyapunov's direct method is addressed followed by theoretical background on integral concurrent learning. A motivational example is presented for a standard nonlinear system.

In Chapter 3, the spacecraft's equations of motion used within the control formulation are presented through the classical and modified equinoctial orbital elements. Moreover, the optical solar pressure model is introduced along with RCDs. Here, a solar irradiance model used in simulation to capture the 11-year solar cycle is considered.

In Chapter 4, the Lyapunov control design is derived in addition to an integral concurrent learning update law for online estimation of the irradiance from the Sun. For this, Gauss' variational equations are employed to model the time rate of change of the spacecraft's orbital elements. Other orbital perturbations due to gravitational effects from neighboring celestial bodies are considered in the proposed formulation. Briefly, global exponential tracking of the estimated parameters and states of interest is proved in this chapter.

In Chapter 5, numerical simulations for two sample missions are considered: (1) a geo-stationary debris removal case and (2) an Earth-Mars interplanetary transfer orbit following a logarithmic spiral reference trajectory. Results are compared to trajectories with no estimation to illustrate the need to account for solar flux fluctuations.

In Chapter 6, remarkable conclusions and future research that will follow this thesis are discussed. The potential to use integral concurrent learning for online estimation of unknown parameters is suggested for solar sailing formation flight maneuvers. Estimation of the thermo-optical film properties is also proposed and encouraged for future investigations.

2 Literature Review and Preliminaries

As the interest in solar sailing continues to increase as a cost effective alternative to traditional propulsion systems, this chapter presents the state of the art in solar sailing guidance, navigation, and control and current challenges in solar-observation studies. A review of adaptive control along with integral concurrent learning is also presented in this chapter.

2.1 Reflectivity Modulation Technology

For a solar sail of fixed geometry and characteristic acceleration, active control is unattainable as the only control variables are given by the sail's attitude [6–8]. In this context, two proposed solutions to this problem are considered in the literature among which solar flux fluctuations are often neglected. One assumes a variable-geometry solar sail model [9], while the second one suggests the implementation of reflectivity modulation technology for orbital control.

Reflectivity modulation technology is adopted for active control of solar sails in accordance with previous demonstration missions and applications [2, 6–8]. A reflectivity control device (RCD) is a device manufactured from electrochromic materials composed of a thin layer of polymer dispersed nematic liquid crystals [10]. Effectively, upon application of a low electric voltage, nematic crystals within the film align with the electric field, allowing its reflectivity coefficient to change from a diffusive to a highly specular state [10]. IKAROS (2010), the world's first successful interplanetary solar sail demonstration mission, employed a reflectivity control device for attitude control [2]. By synchronizing the fraction of switched-on RCDs, the spacecraft was able to change its spinning axis without consuming fuel [18]. RCDs were installed at the periphery of the sail to generate sufficient torque (Figure 2.1). The trajectory of IKAROS was controlled indirectly by its attitude. IKAROS conveniently performed a reverse turn of its angular momentum vector relative to the inertial frame while approaching Venus as part of its mission [2].

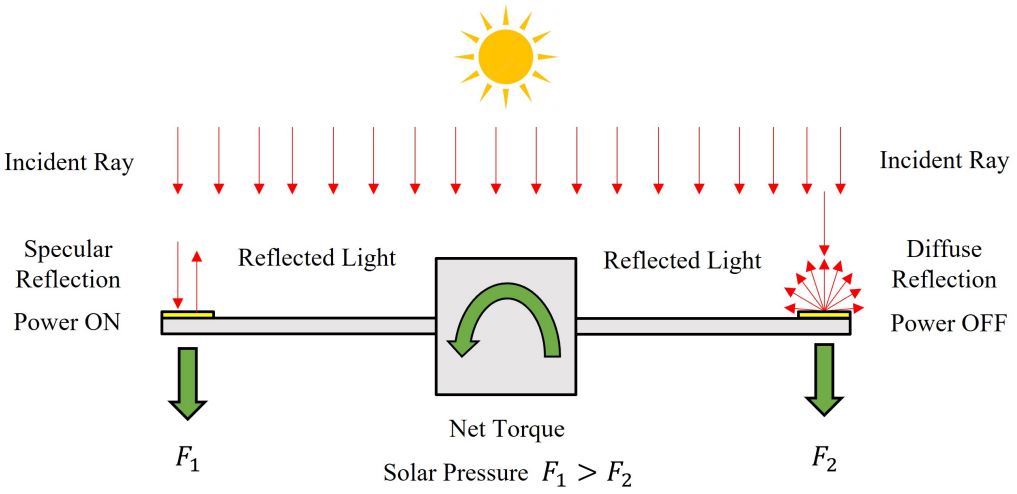

Figure 2.1 Attitude control concept of the IKAROS mission using RCDs [2].

At the present time, a new class of RCDs are under development by the University of Tokyo and JAXA entitled Advanced-RCD or simply A-RCD [10]. Unlike conventional RCDs, A-RCDs deflect the light obliquely to generate a toque perpendicular to the sail's surface to avoid deformation of the solar sail membrane, also referred as the windmill effect. An optimal design of the reflection angle at the oblique reflection film is studied in recent literature for future implementation of an additional degree of freedom [10].

Since the introduction of RCDs for attitude control by its pioneer IKAROS, substantial research on orbital control has been conducted using RCDs. For instance, in Niccolai et al. [6], a full state feedback control law is designed with a linear quadratic regulator (LQR) approach to stabilize an L_1-type artificial equilibrium point using RCDs. Similarly in Mu et al. [7], the application of this technology for solar sail formation flying was investigated for the purpose of tracking a reference trajectory for a magnetosphere mission. Here, the relative solar radiation pressure acceleration was linearized to derive a Lyapunov-based control law followed by a constrained nonlinear predictive controller [7]. It was concluded that small variations in the control variables given by the fraction of switched-on RCDs and the spacecraft attitude was sufficient to track a desired orbit [6, 7].

In Gong and Li [19], RCDs are used to stabilize periodic Halo orbits around Lagrange points within the restricted three-body problem. Here, a linear quadratic regulator, designed for a linearized system about a periodic orbit of interest, was compared to a Floquet theory-based control law. In this study, convergence to a family of Halo orbits was accomplished. Similarly, in Biggs and Negri [20], an orbit-attitude control scheme is proposed to track an artificial equilibrium point of the Earth-Moon system. In contrast to Gong and Li [19], RCDs are both used to control the attitude and orbit of the solar sail simultaneously [20]. Nevertheless, the solar radiation pressure coefficient was assumed to be a constant and known value.

2.2 Total Solar Irradiance Effect

Recent studies have shown the need to account for solar flux fluctuations [13, 14]. Nevertheless, in most academic papers, solar flux fluctuations are often neglected owing to the assumption of a constant solar radiation pressure coefficient. In addition, it is commonly assumed to be a known parameter. As the solar flux is the primary source of momentum exchange of a solar sail, the effect of the actual solar pressure on low-eccentricity and interplanetary orbits was analyzed in Vulpetti [13, 14] using the time series of the total solar irradiance (TSI) as opposed to unreliable TSI models. A storm-warning orbit and an Earth-Mars transfer orbit were considered in these studies.

In Vulpetti [13], interpolation of the daily TSI means was employed within a *Fortran-90* simulation code using the variable-stepsize Adams–Bashforth–Moulton method to study the effect solar flux fluctuations have on low eccentricity orbits. It was assumed that the spacecraft was insensitive to TSI changes with periods shorter than 0.25 days based on the measurable TSI frequency domain from 1978 to 2002 [21]. In addition, the secular variation of the solar activity was neglected as the solar flux has been shown to increase on average 1.3 W/m^2 per century [22]. Since most solar sail missions to consider exhibit operational times much less than a century, only the variation due to the 11-year solar cycle ($0.1-0.2\%$) was part of the daily TSI means recorded [13].

Moreover, as the solar flux measurements given by the PMOD composite TSI time series are adjusted to 1 AU [23], the spacecraft trajectory was propagated without time delay while TSI measurements were scaled by the inverse of the square of the distance from the Sun $(\mathrm{AU}/r_{\odot})^2$ to reconstruct their true values [13]. Gravitational perturbations from the inner planets and Jupiter were considered in this study. A circular warning orbit was considered to observe corona mass ejections that could potentially induce electromagnetic storms. A solar sail spacecraft was proposed as a means to extend the length of the mission and stabilize its Halo orbit around the Sun-Earth L_1 libration point without consuming fuel. Here, the spacecraft's orbital period under variable TSI and constant TSI was compared. Additionally, the effect gravitational perturbations have on the spacecraft orbit due to the inner planets and Jupiter was illustrated. Results indicate that solar flux fluctuations as low as $0.1-0.2\%$ of the mean values produce perturbations 100 times those due to the gravitational interaction between neighboring planets [13].

Correspondingly, in Vulpetti [14], a heliocentric transfer orbit from Earth to Mars was considered within the same large high-precision computer code to study the effect solar flux fluctuations have on the trajectory of a solar sail. The study concluded that solar flux fluctuations produce large perturbations on the spacecraft trajectory over the mission time span [14]. This shows the sensitivity of a solar sail to the variation of the solar flux. The position difference between the trajectory under constant TSI and variable TSI was plotted showing that if solar flux fluctuations are neglected, a solar sail could be hundreds of thousand of kilometers away from the target [13]. As a means to circumvent this problem, the implementation of a solar flux measurement package has been suggested as part of the attitude and orbital control system. For instance, in Caruso et al. [8], a control law was developed to counteract solar flux fluctuation on the optimal heliocentric transfer of a reflectivity-controlled solar sail assuming real-time measurements of the solar flux are available.

For clarification purposes, TSI measurements at a distance of 1 AU are commonly known as absolute solar flux measurements or, equivalently, absolute TSI measurements in the literature [16]. Furthermore, the solar flux and the SRP coefficient are often interchangeable as the SRP coefficient is the solar flux normalized by the speed of light in the vacuum [24].

2.3 Solar Sailing Control with Solar Irradiance Fluctuations

An optimal solar sail control strategy was proposed to counteract both long-term and short-term variations in the irradiance from the Sun [8]. In this study, the heliocentric orbit-to-orbit trajectory that aims to minimize flight time was considered. In this section, a brief summary of the control scheme is discussed. The optical solar pressure model that describes the spacecraft acceleration based on the thermo-optical film properties was employed. RCDs were used to adjust the sail's thrust magnitude. Additionally, the spacecraft cone angle served as an additional variable of this formulation to guarantee tracking and the existence of a solution. More precisely, the spacecraft propulsive acceleration was decomposed into its transverse and radial components in terms of the cone and clock angles relative to the LVLH frame that denote spacecraft orientation.

Given a reference fraction of switched-on RCDs, a constant reference solar radiation pressure coefficient, and reference attitude control angles, the transverse and radial components of the spacecraft acceleration were constrained to their reference values to obtained the required fraction of switched-on RCDs that would counteract the variability of the solar flux from a presumed constant during the preliminary phase of the mission. Ultimately, a nonlinear sixth-order trigonometric equation solves for the required control variables using standard numerical algorithms assuming the clock angle equals it reference value. A detailed discussion on the equations that relate to this approach is presented in Chapter 4. Nevertheless, it was assumed that real-time measurements of the solar flux are available [8]. Furthermore, as this method arises from a mathematical equality, there is no state feedback in this formulation. Indeed, error due to inaccurate solar flux measurements would result in the deviation of the spacecraft from its reference trajectory.

2.4 Total Solar Irradiance Observations

TSI variability is associated to the Sun's surface magnetic behaviour attributed to a convective phenomenon known as granulation. Granulation is the pattern observed on the Sun's surface caused by the convection of plasma just below the photosphere [25]. Additionally, different regions of the Sun rotate at different speeds. Since the plasma near the equator rotates much faster than the plasma at the poles, the difference in the rotational speed causes the magnetic field to flip on average every 11 years [26]. More in detail, since the Sun's hydrogen ions tend to travel along the magnetic field lines, some particles of trapped hot gasses known as sunspots form. This results in irregular but periodic solar activity that translates to the solar flux variability of interest in this study.

Since 1978, absolute radiometers have been onboarded satellites to measure the solar flux variation for solar-observation studies to overcome limitations of ground monitoring [16]. Radiometers onboarded satellites work on the principle of thermal detectors based on heating a black body due to solar radiation absorption [27]. In a vacuum environment, the absorbed radiation that results in a temperature gradient equals the voltage difference in the electrical and optical heating elements. The relationship between these parameters is commonly adjusted via a correction factor to account for uncertainties. More precisely, this also accounts for diffraction losses and the Doppler effect [28, 29].

However, as noted in recent literature, there is no consensus on a single total solar irradiance time series as different radiometers measure inconsistent values due to measurement accuracy, absolute calibration, and altitude corrections [16]. In addition, the long-term TSI variability has not been established as most radiometers do not exceed more than a decade due to material degradation [16]. As a result, the solar flux variation due to the 11-year solar cycle has not been accurately characterized. Composite TSI measurements from multiple instruments are used to reconstruct the long-term variation in this value [23]. However, the stability difference in all sources of uncertainty leads to unreliable TSI measurements and models.

Indeed, accurate solar flux measurements represent a current challenge in the scientific community. The Compact Total Irradiance Monitor-Flight Demonstration (CTIM-FD) mission by NASA is one of the many solar-observation missions in progress that aim to study solar flux variability. The CTIM-FD mission is currently testing future technology for TSI measurements [17]. In addition, the Brazilian Galileo Solar Space Telescope (GSST) aims to study the Sun's evolution of its magnetic structure as well as its impact on the Earth's atmosphere and climate [16].

As reported in Carlesso et al. [16], the accuracy improvement in modern radiometers originates from new material development, data acquisition, feed-forward control systems, and precision aperture location [30]. In this context, modern radiometers are strictly required to feature higher accuracy, stability, and moderate cadence compared to their predecessors. However, it is still unknown and subject of study to characterize the limitations of current technologies. In this sense, a solar flux measurement package part of the attitude and orbital control system, as proposed in the literature to account for solar flux fluctuations, would not be ideal as it would only increase the mission cost and compromise control capabilities. Alternatively, we suggest an adaptive control scheme along with integral concurrent learning that relies on an accurate solar sail model to estimate the irradiance from the Sun.

2.5 Adaptive Control Preliminaries

Within the scope of control theory, adaptive control emerges as a control method to account for uncertainties in dynamical systems [31]. Such uncertainties include external disturbances to the system's model as well as variation in the system's parameters. In general there are two substantial techniques to compensate for such unknown variations. One approach involves a disturbance rejection scheme through a linear combination of known basis functions. Here, the adaptive control policy is formulated to determine, often but not necessarily always, any linear combination of the basis functions to cancel out the disturbance [31].

Another approach involves the convergences of ideal trajectories by estimation of the respective control gains of the control policy that are required to track a reference model while compensating for unknown parameters within the system's state space representation. This approach is commonly referred to as model reference adaptive control (MRAC). In this sense, a family of control strategies suitable for multiple system's structures arises as a combination of these two methods. For instance, the adaptive output feedback regulator and the MRAC with disturbance rejection [31].

Normally, the control law is considered to be indirect if it uses estimated parameters that are constantly being updated. Otherwise, the control law is considered to be direct [31]. To guarantee convergence of the estimated parameters to their true values, one would need to evaluate the persistence of excitation (PE) condition. In simple words, the persistence of excitation condition provides the means to determine whether or not the system's response contains enough information to uniquely estimate the uncertain parameters [32]. In general, for a generic linear system, we require $N/2$ number of distinct frequencies in the input signal to guarantee the convergence of the estimated parameters to their true values, where N denotes the number of uncertain parameters. However, for nonlinear systems, a similar statement is not easily defined. In fact, the PE condition for nonlinear systems cannot be guaranteed a priori and is difficult to check online. In addition, it often compromises guidance as regularly the spacecraft dynamics do not satisfy the PE condition. In mathematical terms, the PE condition for dynamical systems is formally described by the following theorem [32].

Theorem 1.1: Persistence of Excitation for Dynamical Systems

A dynamical system is persistently excited if $\exists\, \alpha > 0$ and $T > 0$ such that

$$\int_{t}^{t+T} \boldsymbol{y}(\tau)\boldsymbol{y}^{T}(\tau)\,\mathrm{d}\tau \;>\; \alpha I_{N\times N} \quad \forall\, t \tag{2.1}$$

where $\boldsymbol{y}(t)$ is a vector function used for parameters estimation and I is the identity matrix.

As a result, concurrent learning (CL) is used to estimate and account for uncertainties and variation over time in unknown parameters without satisfying the common persistence of excitation condition. More precisely, integral concurrent learning (ICL) is suggested as a modified CL formulation with better tracking and estimation performance in which estimation of the states derivatives is not required [12]. To better illustrate this, let us briefly discuss Lyapunov's direct and indirect methods, which serve as the foundation to most adaptive control strategies including integral concurrent learning.

2.5.1 Lyapunov Indirect Method

Lyapunov's indirect method, applicable only for time-invariant systems, involves the linearization of a nonlinear system about an equilibrium point to study the system's stability within a neighborhood of the equilibrium based on the eigenvalues of the state matrix $\sigma(A) = \{\lambda\}_{i-1}^{n}$. More precisely, the following conclusions can be made based on the eigenvalues of the state matrix A [31].

- If the state matrix A is Hurwitz, meaning $Re(\lambda_i) < 0 \ \ \forall \ \ \lambda = 1, 2, ..., n$, then the system is locally asymptotically stable in the neighborhood of the equilibrium point.
- If $Re(\lambda_i) > 0$ for any $\lambda = 1, 2, ..., n$, then the equilibrium point is unstable for the nonlinear system.
- If $Re(\lambda_i) \leqslant 0 \ \ \forall \ \ \lambda = 1, 2, ..., n$, we cannot draw any conclusions about the equilibrium point of the nonlinear system.

Consequently, for nonlinear systems, as is the case of the governing equations of a solar sail, we often required a more powerful method to determine stability properties.

2.5.2 Lyapunov Direct Method

Lyapunov's direct method serves as a energy-based principle that determines the stability of a nonlinear system based on the response of a user-defined scalar positive definite function $V(\boldsymbol{x}(t))$ to the evolution of the states over time $\boldsymbol{x}(t)$. Such evolution of $V(\boldsymbol{x}(t))$ is determined by the negative definiteness of its continuous first order time derivative [31].

- if $\dot{V}(\boldsymbol{x}(t)) \leqslant 0 \ \ \forall \ \ \boldsymbol{x}(t) \neq 0$ and $\| \ \boldsymbol{x} \ \| < R \in \Re^{+}$, then the origin is locally stable $\forall \ \| \ \boldsymbol{x}(t) \ \| < R$.
- if $\dot{V}(\boldsymbol{x}(t)) < 0 \ \ \forall \ \ \boldsymbol{x}(t) \neq 0$ and $\| \ \boldsymbol{x}(t) \ \| < R \in \Re^{+}$, then the origin is locally asymptotically stable $\forall \ \| \ \boldsymbol{x}(t) \ \| < R$.
- Additionally, if $\dot{V}(\boldsymbol{x}(t)) < 0 \ \ \forall \ \ \boldsymbol{x}(t) \neq 0$ and $V(\boldsymbol{x}(t))$ is radially unbounded, then the origin is globally asymptotically stable.

However, if your choice of $V(\boldsymbol{x}(t))$ fails to prove stability for any of these conditions, no conclusion can be made about the stability of the equilibrium. Moreover, we often require Barbalat's Lemma to further extend the stability conclusion about the states or tracking error to the origin.

Theorem 1.2: Barbalat's Lemma

Barbalat's Lemma states that if the Lyapunov's candidate function is bounded and it first derivative is uniformly continuous (e.i., $\ddot{V}$ is bounded), then $\dot{V}(\boldsymbol{x}(t)) \rightarrow 0$ as $t \rightarrow \infty$. This sometimes implies that the states, or equivalently, the tracking error converges to the origin [31]. Alternatively, all trajectories are bounded if:

- $W_1(\boldsymbol{x}) \leqslant V(\boldsymbol{x}, t) \leqslant W_2(\boldsymbol{x})$.
- $\dot{V}(\boldsymbol{x}, t) \leqslant -W_3(\boldsymbol{x}) \leqslant 0$ for some $W_3(\boldsymbol{x}) > 0$.

where $W_1(\boldsymbol{x})$ and $W_2(\boldsymbol{x})$ are positive definite decrescent functions. Furthermore, $W_3(\boldsymbol{x}) \rightarrow 0$ as $t \rightarrow \infty$, which sometimes implies that $\boldsymbol{x} \rightarrow 0$ as $t \rightarrow \infty$, if $W_3(\boldsymbol{x})$ is uniformly continues.

In fact, integral concurrent learning uses the principles of Lyapunov's direct method to guarantee global asymptotic tracking of the estimated parameters and states in conjunction with Barbalat's Lemma. More in detail, derivation of the respective update law that dictates the rate of adaptation of the uncertain parameters is partially derived from Lyapunov's direct method. A motivational example is presented to show how one can relax the PE condition and still guarantee parameter convergence.

2.6 Integral Concurrent Learning

Integral concurrent learning is an online adaptive update scheme that guarantees convergence of uncertain parameters without the persistence of excitation condition. More precisely, integral concurrent learning is suggested as a modified CL formulation with better tracking and estimation performance in which estimation of the states derivatives is not required [12]. Recorded data are exploited in the update law while numerical integration is used to determine the relationship between the estimation error and the measurable states available. In this way, the update law results in negative definite error terms in the Lyapunov analysis. An online verifiable finite excitation condition based on the minimum eigenvalue of the summation serves as a real-time convergence criteria [12].

In contrast to other adaptive control schemes, integral concurrent learning is suitable for countless numbers of engineering problems disregarding the system's structure and dimensions. However, to properly apply the fundamental theorem of calculus to the equations of motion to model the relationship between the estimation error and the measurable states available, we require the uncertain parameters to be scalar constants [12]. Additionally, a dependent linear parameterization of the uncertain parameters, given a finite set of basis functions, is necessary. Integral concurrent learning fails given an independent set of uncertain parameters that would perturb the system by different means. For instance, one might not use integral concurrent learning to simultaneously estimate the uncertain parameters within the SRP acceleration of a solar sail while estimating the harmonic coefficients of the Earth's gravitational potential function.

To the author's knowledge, integral concurrent learning has only been used for online estimation of spacecraft systems to account for uncertainties in a differential drag-based device and in the mechanical properties of flexible spacecraft. More in detail, in Riano-Rios et al. [33], an integral concurrent learning update law was implemented to estimate the atmospheric density, drag coefficient, and physical properties of a differential drag-based spacecraft to perform formation flight maneuvers and rendezvous applications for cases in which we might not know the chief's acceleration. Moreover, recent research shows the application of integral concurrent learning to estimate the stiffness of flexible spacecraft structures using Kane's equation [34].

To better illustrate the fundamental idea of integral concurrent learning, we consider a motivational example for a standard nonlinear system. Here, we consider a modification of the system found in Parikh et al. [12]. However, in contrast to Parikh's work, we will excite the system to a different reference input signal to show the benefit of using integral concurrent learning to relax the persistence of excitation condition.

2.6.1 Motivational Example

For demonstration purposes, we consider the following time-varying nonlinear system model in state space form.

$$\dot{\boldsymbol{x}}(t) = \boldsymbol{f}(\boldsymbol{x}(t), t) + \boldsymbol{u}(t) \tag{2.2}$$

where $\boldsymbol{x}(t) \in \Re^n$ is the system's states and $\boldsymbol{u}(t) \in \Re^n$ the system's input. We assume the system's uncertain parameters $\boldsymbol{\theta} \in \Re^m$ are linearly parameterized from the regressor matrix $Y(\boldsymbol{x}(t), t) \in \Re^{n \times m}$ such that

$$\dot{\boldsymbol{x}}(t) = Y(\boldsymbol{x}, t)\boldsymbol{\theta} + \boldsymbol{u}(t) \tag{2.3}$$

As common practice, we start by defining a positive definite scalar value Lyapunov candidate function as follows.

$$V(\boldsymbol{e}(t), \Delta\boldsymbol{\theta}(t)) = \frac{1}{2}\boldsymbol{e}^T(t)K\boldsymbol{e}(t) + \frac{1}{2}\Delta\boldsymbol{\theta}^T(t)\Gamma^{-1}\Delta\boldsymbol{\theta}(t) > 0 \tag{2.4}$$

where $\boldsymbol{e}(t) \triangleq \boldsymbol{x}(t) - \boldsymbol{x}_d(t)$ and $\Delta\boldsymbol{\theta}(t) \triangleq \boldsymbol{\theta} - \hat{\boldsymbol{\theta}}(t)$ are the tracking and estimation error, respectively. Here, $\hat{\boldsymbol{\theta}}(t)$ are the estimated parameters and $\boldsymbol{x}_d(t)$ are the desired states. $\Gamma \in \Re^{m\times m}$ is a positive definite control gain matrix used to adjust the rate of adaptation of $\hat{\boldsymbol{\theta}}(t)$, while $K \in \Re^{n\times n}$ is a positive definite state feedback control gain matrix. From here, assuming the uncertain parameters $\boldsymbol{\theta}$ are constant, we differentiate the tracking and estimation errors to obtain the following expressions.

$$\Delta\dot{\boldsymbol{\theta}}(t) = -\dot{\hat{\boldsymbol{\theta}}}(t) \tag{2.5}$$

$$\dot{\boldsymbol{e}}(t) = \dot{\boldsymbol{x}}(t) - \dot{\boldsymbol{x}}_d(t) \tag{2.6}$$

By differentiating Equation (2.4) and rearranging after substituting for the error and system's dynamics in Equation (2.3), (2.5), and (2.6), we obtain the following Lyapunov function time derivative.

$$\dot{V}(\boldsymbol{e}(t), \Delta\boldsymbol{\theta}(t)) = [Y(\boldsymbol{x}(t), t)\hat{\boldsymbol{\theta}} + \boldsymbol{u} - \dot{\boldsymbol{x}}_d(t)]^T\boldsymbol{e} + \Delta\boldsymbol{\theta}^T[(Y(\boldsymbol{x}(t), t)^T\boldsymbol{e}(t) - \Gamma^{-1}\dot{\hat{\boldsymbol{\theta}}}(t)] \tag{2.7}$$

We remove the unknown estimation error dependency in Equation (2.7) by forcing the second term in this equation to be equal to zero while solving for the required update law.

$$\dot{\hat{\boldsymbol{\theta}}}(t) = \Gamma Y(\boldsymbol{x}(t), t)^T\boldsymbol{e}(t) \tag{2.8}$$

Additionally, to initially guarantee boundedness of both states and estimated parameters using the Lyapunov direct method, we design the following control policy.

$$\boldsymbol{u}(t) \triangleq \dot{\boldsymbol{x}}_d(t) - Y(\boldsymbol{x}(t))\hat{\boldsymbol{\theta}}(t) - K\boldsymbol{e}(t) \tag{2.9}$$

Then, the Lyapunov function time derivative becomes the following:

$$\dot{V}(\boldsymbol{e}(t), \Delta\boldsymbol{\theta}(t)) = -\boldsymbol{e}^T(t)K\boldsymbol{e}(t) \leqslant 0 \tag{2.10}$$

Even though $V(\boldsymbol{e}(t), \Delta\boldsymbol{\theta}(t))$ is radially unbounded, global asymptotic tracking is not guaranteed at first as the Lyapunov function time derivative is not negative definite. However, by further extending the stability analysis using Barbalat's Lemma, we conclude that $\boldsymbol{e}(t) \to 0$ as $t \to \infty$. For a visual representation, consider the following desired trajectory.

$$\boldsymbol{x}_d(t) = \begin{bmatrix} 10(1 - e^{-0.1t}) \\ 4(1 - e^{-0.1t}) \end{bmatrix} \tag{2.11}$$

Additionally, assume the regression matrix and uncertain parameters are the following:

$$Y(\boldsymbol{x}(t), t)\boldsymbol{\theta} = \begin{bmatrix} x_1^3(t) & \sin(x_2(t)) & 0 & 0 \\ 0 & x_2(t)\sin(t) & x_1(t) & x_1(t)x_2(t) - t \end{bmatrix} \begin{bmatrix} 5 \\ 10 \\ 15 \\ 20 \end{bmatrix} \tag{2.12}$$

By selecting $\Gamma = 3I_{4\times4}$ and $K = I_{2\times2}$, where I is the identity matrix, we observed that some of the estimated parameters do not converge to their true values (Figure 2.2). Furthermore, tracking to the reference trajectory is not perfect as the control scheme does not result in a valid linear combination of the regressor matrix to compensate for the unknown parameters (Figure 2.3). For this example, the states and estimated parameters were initialized to zero in a *Matlab* simulation code.

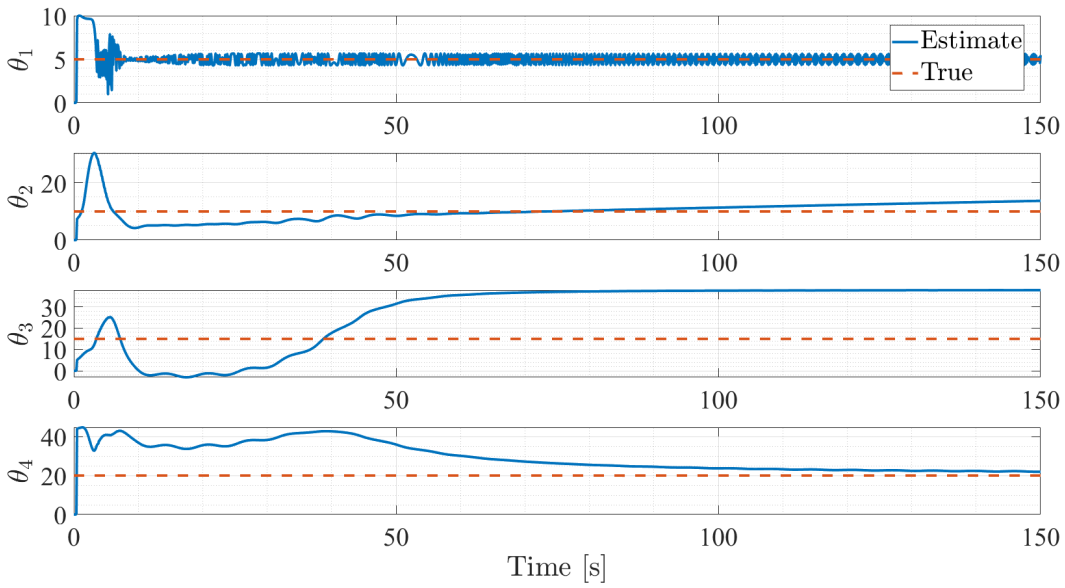

Figure 2.2 Estimated parameters given Lyapunov-based update law.

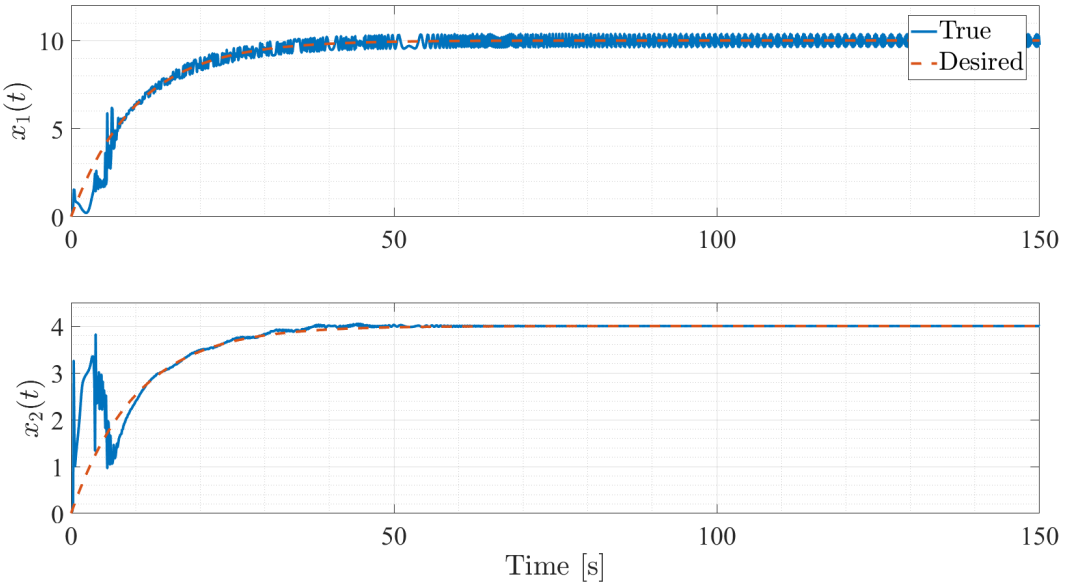

Figure 2.3 System's states under Lyapunov-based dynamics.

However, in an attempt to improve transient performance and increase robustness, integral concurrent learning is introduced to the original update law given by Equation (2.8).

$$\dot{\hat{\boldsymbol{\theta}}}(t) = \Gamma Y(\boldsymbol{x}(t), t)^T \boldsymbol{e}(t) + k_{ICL}\Gamma \sum_{i=1}^{N} \mathcal{Y}_i^T \mathcal{Y}_i \Delta\boldsymbol{\theta} \tag{2.13}$$

Here, K_{ICL} is a matrix control gain used to weight the ICL component of the update law against the Lyapunov-based term. If we assume that the system is sufficiently excited over a finite duration of time $T \in \Re$ such that

$$\lambda_{min} \left\{ \sum_{i=1}^{N} \mathcal{Y}_i^T \mathcal{Y}_i \Delta\boldsymbol{\theta} \right\} \geqslant \bar{\lambda} \quad \forall\, t \geqslant T \tag{2.14}$$

then global asymptotic tracking of the estimated parameters is guaranteed by Theorem 4.10 in the work of Khalil [32]. Here, $\lambda_{min}\{\cdot\}$ is the minimum eigenvalue of the summation and $\bar{\lambda} \in \Re^+$ is an user-defined threshold. Nevertheless, the update law is Equation (2.13) depends on the estimation error, which is intuitively unknown for practical implementation. Therefore, a novel approach whose principles rely upon the fundamental theorem of calculus facilitates an expression of the update law that only depends on measurable input-to-output data. For this, we proceed to integrate Equation (2.3) for the time window $[t - \Delta t, t]$.

$$\int_{t-\Delta t}^{t} \dot{\boldsymbol{x}}(\tau)\, \mathrm{d}\tau = \int_{t-\Delta t}^{t} Y(\boldsymbol{x}(\tau), \tau)\boldsymbol{\theta}\, \mathrm{d}\tau + \int_{t-\Delta t}^{t} \boldsymbol{u}(\tau)\, \mathrm{d}\tau \tag{2.15}$$

Consequently, by applying the fundamental theorem of calculus, we obtain the following:

$$\boldsymbol{x}(t) - \boldsymbol{x}(t - \Delta t) = \mathcal{Y}(t)\boldsymbol{\theta} + \boldsymbol{\mathcal{U}}(t) \tag{2.16}$$

where $\mathcal{Y}(t)$ and $\boldsymbol{\mathcal{U}}(t)$ are defined as follows

$$\mathcal{Y}(t_i) = \int_{t-\Delta t}^{t} Y(\boldsymbol{x}(\tau), \tau)\, \mathrm{d}\tau \tag{2.17}$$

$$\boldsymbol{\mathcal{U}}(t_i) = \int_{t-\Delta t}^{t} \boldsymbol{u}(\tau)\, \mathrm{d}\tau \tag{2.18}$$

Notice that we can pull out from the integral the uncertain parameters $\boldsymbol{\theta}$ as they are assumed to be constant. Therefore, after substituting $\boldsymbol{\theta} = \Delta\boldsymbol{\theta} + \hat{\boldsymbol{\theta}}$, we obtain an equivalent expression of the update law in Equation (2.13) that only depends on the current and previous measured states that accumulate within the summation to relax the persistence of excitation condition to a finite excitation condition.

$$\dot{\hat{\boldsymbol{\theta}}}(t) = \Gamma Y(\boldsymbol{x}(t), t)^T \boldsymbol{e}(t) + k_{ICL}\Gamma \sum_{i=1}^{N} \boldsymbol{\mathcal{Y}}_i^T (\boldsymbol{x}(t_i) - \boldsymbol{x}(t_i - \Delta t) - \boldsymbol{\mathcal{U}} - \mathcal{Y}\hat{\boldsymbol{\theta}}) \tag{2.19}$$

A Matlab simulation of the system considered in the previous example, initialized to the same initial conditions, shows the system's response for a choice of $K_{ICL} = 0.2I$. Here, we now observed better tracking as the estimates converge to their true values.

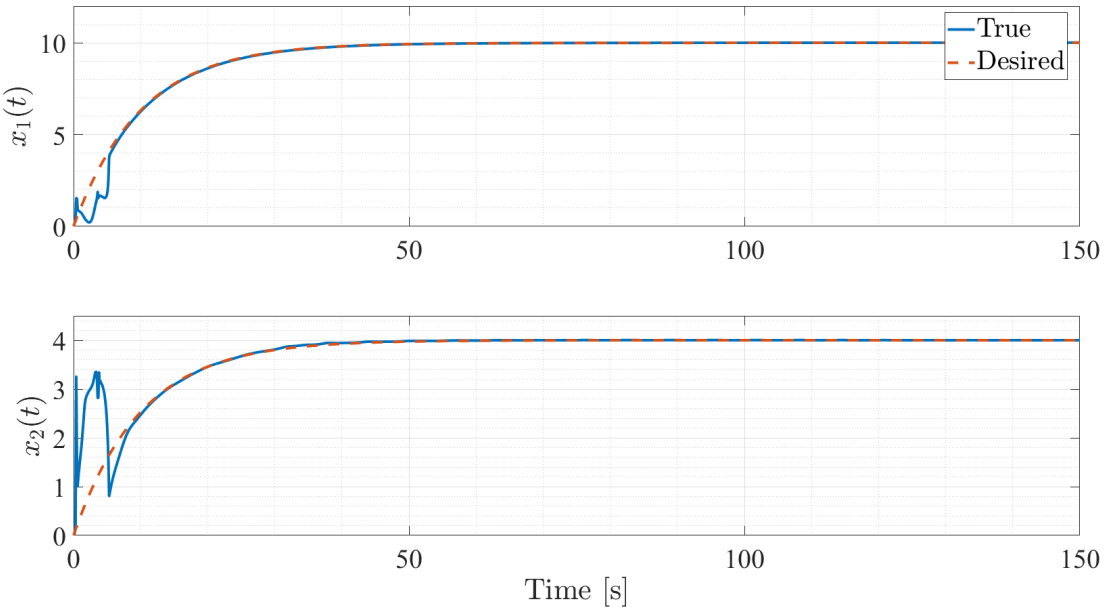

Figure 2.4 System's states under Lyapunov-based dynamics with ICL.

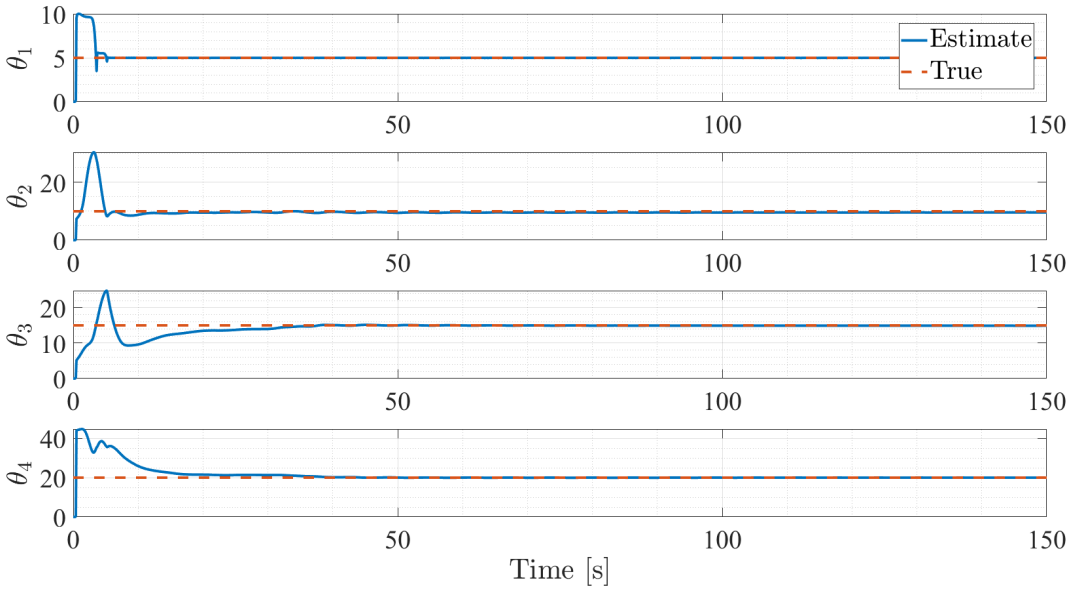

Figure 2.5 Estimated parameters given Lyapunov-based update law with ICL.

3 Dynamic Modeling

3.1 The Two-Body Equations of Motion

The spacecraft's equations of motion can be expressed in the Earth-Centered Inertial (ECI) coordinate system given by the following equation. Equivalently, without loss of generality, the Heliocentric Inertial (HCI) reference frame is commonly used for interplanetary missions.

$$\ddot{\boldsymbol{r}} = -\frac{\mu}{r^3}\boldsymbol{r} + \boldsymbol{a}_{srp} + \boldsymbol{a}_d \tag{3.1}$$

Here, $\boldsymbol{r}$ is the spacecraft position vector and μ is the gravitational parameter of the primary body. $\boldsymbol{a_{srp}}$ is the spacecraft acceleration due to solar radiation pressure while $\boldsymbol{a_d}$ is the disturbance due to other orbital perturbations such as the gravitational effects due to neighboring celestial bodies.

3.2 Classical Orbital Elements

For convenience, the spacecraft's state vector is expressed in terms of the classical orbital elements $\boldsymbol{q}(t)$: semi-major axis (a), eccentricity (e), inclination (i), right ascension of the ascending node (Ω), argument of periapsis (ω), and true anomaly (υ). Gauss' variational equations (GVEs) provides the time rate of change of the orbital elements as a function of the disturbance acceleration [24], including solar radiation pressure.

$$\frac{da}{dt} = \frac{2}{n\sqrt{1-e^2}}\left[e\sin(\upsilon)P_r + \frac{p}{r}P_s\right] \tag{3.2a}$$

$$\frac{de}{dt} = \frac{\sqrt{1-e^2}}{na}\left[\sin(\upsilon)P_r + \left(\cos(\upsilon) + \frac{e+\cos(\upsilon)}{1+e\cos(\upsilon)}\right)P_s\right] \tag{3.2b}$$

$$\frac{di}{dt} = \frac{r\cos(u)}{na^2\sqrt{1-e^2}}P_w \tag{3.2c}$$

$$\frac{d\Omega}{dt} = \frac{r\sin(u)}{na^2\sin(i)\sqrt{1-e^2}}P_w \tag{3.2d}$$

$$\frac{d\omega}{dt} = \frac{\sqrt{1-e^2}}{nae}\left[-\cos(\upsilon)P_r + \sin(\upsilon)\left(1+\frac{r}{p}\right)P_s\right] - \frac{r\cot(i)\sin(u)}{h}P_w \tag{3.2e}$$

$$\frac{d\upsilon}{dt} = \frac{p\cos(\upsilon)}{eh}P_r - (p+r)\sin(\upsilon)P_s + \frac{h}{r^2} \tag{3.2f}$$

where u is the argument of latitude, h is the magnitude of angular momentum, n is the mean motion, and p is the orbit's semi-latus rectum. The disturbance acceleration is described in the Local-Vertical-Local-Horizontal (LVLH) coordinate system centered at the spacecraft's center of mass along the in-track (P_r), cross-track (P_s), and normal components (P_w) as illustrated in Figure 3.1.

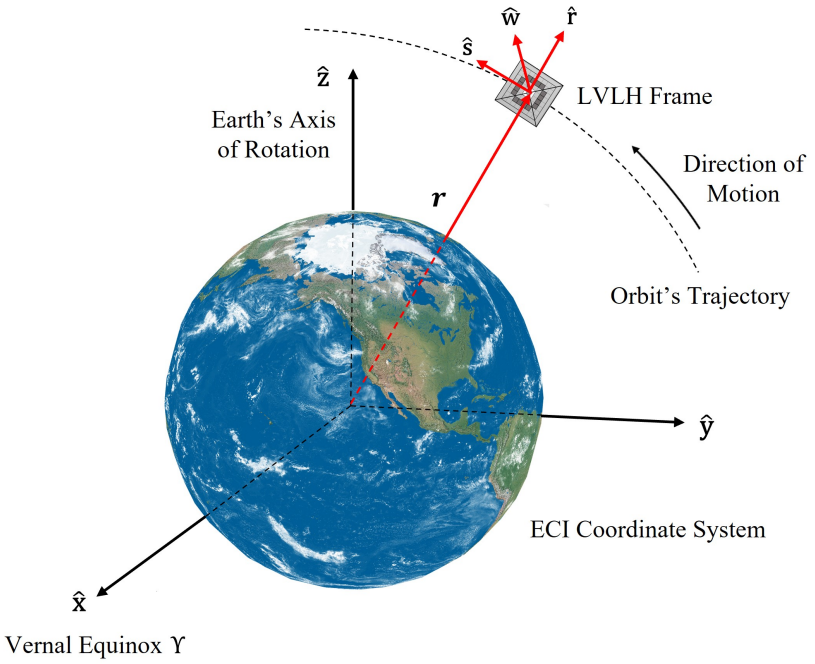

Figure 3.1 LVLH reference frame relative to ECI coordinate system.

3.3 Local-Vertical-Local-Horizontal Reference Frame

More precisely, the disturbance acceleration along the in-track $\hat{\boldsymbol{r}}$, cross-track $\hat{\boldsymbol{s}}$, and normal components $\hat{\boldsymbol{w}}$ is computed from the spacecraft position $\boldsymbol{r}$ and velocity $\boldsymbol{v}$ vectors as expressed in the Earth-Centered Inertial reference frame [35]. This coordinate transformation denotes a right-hand basis system as follows.

$$\hat{\boldsymbol{r}} = \frac{\boldsymbol{r}}{\| \boldsymbol{r} \|} \tag{3.3a}$$

$$\hat{\boldsymbol{w}} = \frac{\boldsymbol{r} \times \boldsymbol{v}}{\| \boldsymbol{r} \times \boldsymbol{v} \|} \tag{3.3b}$$

$$\hat{\boldsymbol{s}} = \hat{\boldsymbol{w}} \times \hat{\boldsymbol{r}} = \frac{(\boldsymbol{r} \times \boldsymbol{v}) \times \boldsymbol{r}}{\| (\boldsymbol{r} \times \boldsymbol{v}) \times \boldsymbol{r} \|} \tag{3.3c}$$

In this sense, Q denotes the transformation matrix. Consequently, the spacecraft's non-two-body perturbations, often modeled in the Earth-Centered Inertial coordinate system, are readily available from Equation (3.5).

$$Q(\boldsymbol{r}, \boldsymbol{v}) = \begin{bmatrix} \hat{\boldsymbol{r}} & \hat{\boldsymbol{s}} & \hat{\boldsymbol{w}} \end{bmatrix} \tag{3.4}$$

$$\begin{Bmatrix} \hat{\boldsymbol{r}} & \hat{\boldsymbol{s}} & \hat{\boldsymbol{w}} \end{Bmatrix}^T = Q^T \begin{Bmatrix} \hat{\boldsymbol{x}} & \hat{\boldsymbol{y}} & \hat{\boldsymbol{z}} \end{Bmatrix}^T \tag{3.5}$$

3.4 Modified Equinoctial Orbital Elements

To avoid singularities in GVEs due to circular orbits ($e = 0$) and equatorial orbits ($i = 0^\circ, 180^\circ$), the modified equinoctial orbital elements (MEOE) are often used for trajectory analysis and optimization problems [36–38]. The following set of equations, valid for circular, elliptical, and hyperbolic orbits, provide the relationship between MEOE and COE.

$$p = a(1 - e^2) \tag{3.6a}$$

$$f = e\cos(\omega + \Omega) \tag{3.6b}$$

$$g = e\sin(\omega + \Omega) \tag{3.6c}$$

$$h = \tan\left(\frac{i}{2}\right)\cos(\Omega) \tag{3.6d}$$

$$k = \tan\left(\frac{i}{2}\right)sin(\Omega) \tag{3.6e}$$

$$L = \Omega + \omega + \theta \tag{3.6f}$$

Here, L denotes the true longitude. In this sense, the spacecraft dynamics are described by the following first-order time-varying nonlinear equations of orbital motion [36].

$$\boldsymbol{q}_m(t) = \begin{bmatrix} p & f & g & h & k & L \end{bmatrix}^T \tag{3.7}$$

$$\frac{d\boldsymbol{q}_m}{dt} = A(\boldsymbol{q_m})\boldsymbol{P} + \boldsymbol{b} \tag{3.8}$$

Analogously to GVEs, they provide the time rate of change of the modified equinoctial orbital elements as a function of the disturbance acceleration acting on the spacecraft. For simplicity, we define the state vector and its corresponding dynamics in matrix form where A and $\boldsymbol{b}$ are defined as follows.

$$A = \begin{bmatrix} 0 & \frac{2p}{w}\sqrt{\frac{p}{\mu}} & 0 \\ \sqrt{\frac{\mu}{p}}\sin(L) & \sqrt{\frac{\mu}{p}}\frac{1}{w}[w+1\cos(L)+f] & \sqrt{\frac{\mu}{p}}\frac{g}{w}[h\sin(L)-k\cos(L)] \\ -\sqrt{\frac{\mu}{p}}\cos(L) & \sqrt{\frac{\mu}{p}}[w+1\sin(L)+g] & \sqrt{\frac{\mu}{p}}\frac{f}{w}[h\sin(L)-k\cos(L)] \\ 0 & 0 & \sqrt{\frac{\mu}{p}}\frac{s^2\cos(L)}{2w} \\ 0 & 0 & \sqrt{\frac{\mu}{p}}\frac{s^2\sin(L)}{2w} \\ 0 & 0 & \sqrt{\frac{\mu}{p}}[h\sin(L)-k\cos(L)] \end{bmatrix} \tag{3.9}$$

$$\boldsymbol{b} = \begin{bmatrix} 0 & 0 & 0 & 0 & 0 & \sqrt{\mu p}\left(\frac{w}{p}\right)^2 \end{bmatrix}^T \tag{3.10}$$

Here, α, s, and w are auxiliary variables defined in Appendix A.

3.5 Orbital Perturbations

The orbital perturbations to considered in this study include the gravitational effects due to neighboring celestial bodies in addition to gravitational perturbations due to the Earth's oblateness when applicable. In this section, we present the mathematical expressions required to model these perturbations in simulation.

3.5.1 Solar and Lunar Gravity

Given the geocentric equatorial position of the three-body system considered, the absolute acceleration due to the mutual interaction among them provides the acceleration acting on the spacecraft due to the third body [35]. Here, we separately consider the Moon ☾ and the Sun ☉ as the third body. For instance, let $\boldsymbol{r}_{☾/S}$ be the Moon's position vector relative to the spacecraft and $\mu_☾$ be the Moon's gravitational parameter. The Moon's geocentric position $\boldsymbol{r}_☾$ is captured through a low-precision algorithm using the formulas presented in *The Astronomical Almanac* [39]. In the context, the acceleration due to the Moon's gravity is obtained as

$$\boldsymbol{a}_{\leftmoon} = \mu_{\leftmoon} \left(\frac{\boldsymbol{r}_{\leftmoon/S}}{r^3_{\leftmoon/S}} - \frac{\boldsymbol{r}_{\leftmoon}}{r^3_{\leftmoon}} \right) \tag{3.11}$$

Similarly, one might characterize the gravitational pull from the Sun. However, for near-Earth applications, as the spacecraft distance to the Sun is virtually equal to the Earth-Sun distance, a mathematical manipulation of this equation is required to accurately compute the difference between these two values using a finite precision computer. To this extent, the Sun's gravitational influence on the spacecraft is rewritten in an equivalent form to minimize roundoff error [35].

$$\boldsymbol{a}_{\odot} = \frac{\mu_{\odot}}{r^3_{\odot/s}} \left[F(\psi)\boldsymbol{r}_{\odot} - \boldsymbol{r} \right] \tag{3.12}$$

where $\mu_{\odot}$ is the Sun's gravitational parameter, $r_{\odot/s}$ is the Sun's relative position to the spacecraft given its inertial position $\boldsymbol{r}_{\odot}$, while $F(\psi)$ and ψ are defined as follows.

$$F(\psi) = \frac{\psi^2 - 3\psi + 3}{1 + (1-\psi)^{3/2}}\psi \tag{3.13}$$

$$\psi = \frac{\boldsymbol{r} \cdot (2\boldsymbol{r}_{\odot} - \boldsymbol{r})}{r^2_{\odot}} \tag{3.14}$$

3.5.2 Earth's Harmonics

The Earth's non-two-body effect is captured through the second zonal and tesseral harmonics using the following gravitational potential function [15, 24].

$$U = \frac{\mu_{\oplus}}{r} \left(\frac{R_{\oplus}}{r} \right)^2 \left[3C_{2,2} \frac{x^2 + y^2}{r} - \frac{1}{2} C_{2,0} \left(1 - 3\frac{z^2}{r^2} \right) \right] \tag{3.15}$$

Here, $\mu_{\oplus}$ is the Earth's gravitational parameter and $R_{\oplus}$ is the Earth's mean radius. $\{x\ y\ z\}^T$ denotes the Cartesian components of the position vector. $C_{2,2}$ and $C_{2,0}$ are the second tesseral and zonal harmonic coefficients that capture the Earth's oblateness and irregularities due to non-spherical regions.

3.6 Optical Solar Pressure Model

For the purpose of this research, the following model, adopted from Reference [3] and modified a posteriori in Reference [8] with reflectivity modulation technology, features RCDs for active control of a solar sail considering the optical solar pressure model (Figure 3.2).

$$\boldsymbol{a}_{srp} = \frac{V P_{srp} A_{tot} \cos(\phi_{inc})}{m} \left(\frac{\mathrm{AU}}{r_{\odot}}\right)^2 [b_1 \hat{\boldsymbol{e}}_{\odot} + (b_2 \cos(\phi_{inc}) + b_3)\hat{\boldsymbol{n}}] \tag{3.16}$$

Here, m is the spacecraft's mass, P_{srp} is the local time-varying solar radiation pressure coefficient at a distance of 1 AU, $\hat{\boldsymbol{e}}_{\odot}$ is the Sun's position unit vector, V is the shadow coefficient given by the conical shadow model [24], ϕ_{inc} is the sail's incidence angle, and $r_{\odot}$ is the sail's distance from the Sun. $\{b_1, b_2, b_3\}$ are the dimensionless force coefficients defined in terms of the thermo-optical film properties.

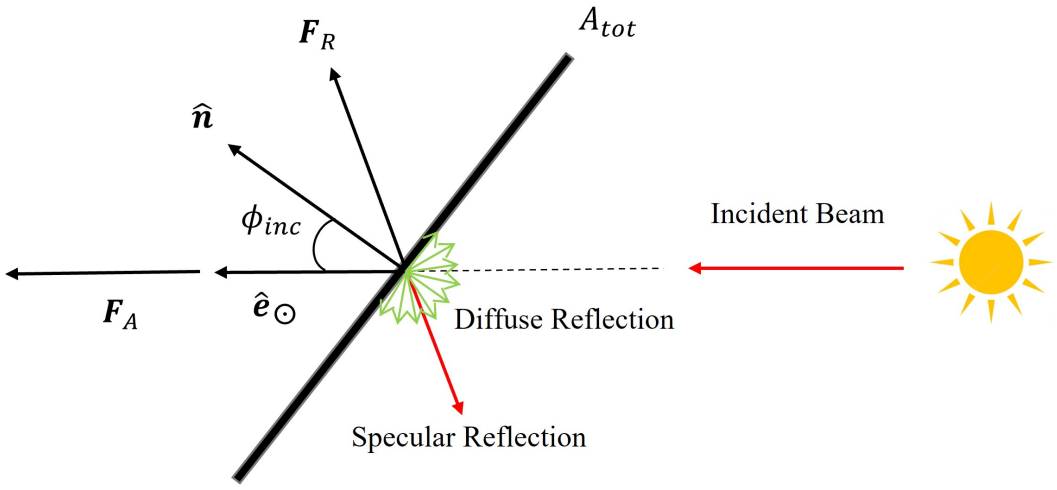

Figure 3.2 Solar sail illustration of sunlight reflection for a flat plate model.

$$b_1 = 1 - \tilde{r}s \tag{3.17a}$$

$$b_2 = 2\tilde{r}s \tag{3.17b}$$

$$b_3 = B_f\tilde{r}(1-s) + (1-\tilde{r})\frac{\epsilon_f B_f - \epsilon_b B_b}{\epsilon_f + \epsilon_b} \tag{3.17c}$$

where $\tilde{r}$ is the reflection coefficient, s is the fraction of photons specularly reflected, B_f (or B_b) is the non-Lambertian coefficient of the front (or back) surface, and ϵ_f (or ϵ_b) is the film emissivity of the front (or back) surface.

3.6.1 Reflectivity Control Device

As explained in Caruso et al. [8], it is assumed that sunlight is diffusively reflected when the device is switched-off and specularly reflected in its on-state (Figure 3.3). It is assumed that only a small fraction of the total sail area A_{tot} has RCDs installed. Consequently, we defined A_s as the aluminized film area and A_{RCD}^{on} as the area covered by switched-on RCDs. In this sense, assuming the optical properties of the aluminized film area coincide with those of the switched-on RCDs, we introduce $f \in [A_s/A_{tot}, 1]$ as the reflectivity modulation ratio, defined as the fraction of the sail area in highly reflective mode. In practice, assuming there are sufficiently many small RCDs, f can vary accordingly from A_s/A_{tot} to 1 continuously.

$$f = \frac{A_s + A_{RCD}^{on}}{A_{tot}} \tag{3.18}$$

$f = A_s/A_{tot}$ would imply that all RCDs are switched-off. On the other hand, $f = 1$ physically denotes that all RCDs are switched-on and that the entire sail area experiences specular-dominant reflection. In this context, the reflectivity modulation ratio along with the sail's orientation, denoted by the sail's surface normal vector opposite to the Sun $\hat{\boldsymbol{n}}$

(Figure 3.2), constitute the two control variables of this formulation to independently adjust the thrust magnitude and direction, respectively. The dimensionless force coefficients b_i, with $i = \{1, 2, 3\}$, in the presence of RCDs now become

$$b_i = f b_i^{on} + (1 - f) b_i^{off} \tag{3.19}$$

In the presented work, the thermo-optical film properties of the NEA Scout mission are used to calculate the dimensionless force coefficients characteristic of the highly reflective mode [40]. Instead, for the switched-off RCDs, Lambertian diffusion is assumed [24] (Table 3.1).

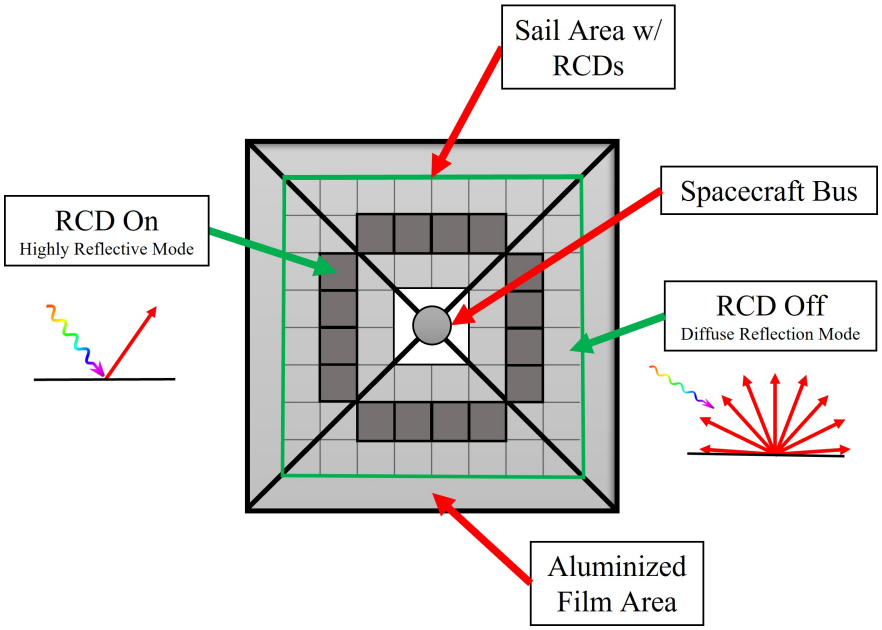

Figure 3.3 Solar sail schematic with reflectivity modulation technology.

Table 3.1 Thermo-optical film properties

Description	Symbol	Switched-On State	Switched-Off State
Reflection Coefficient	$\tilde{r}$	0.91	1
Fraction of Photons Specularly Reflected	s	0.89	0
Non-Lambertian Coefficient (Front)	B_f	0.79	2/3
Non-Lambertian Coefficient (Back)	B_b	0.67	$\sim$
Emissivity (Front)	ϵ_f	0.025	$\sim$
Emissivity (Back)	ϵ_b	0.27	$\sim$

3.6.2 Solar Irradiance Model

Inspired by the results of Riano-Rios et al. [33], where the atmospheric density of a differential drag-based spacecraft was modeled using its two principal Fourier components, the true solar radiation pressure coefficient is modeled as a linear combination of two parameters at a certain frequency. More precisely, one can assume a sinusoid of period of 11 years to characterize the solar flux variation due to the solar cycle.

$$P_{srp} = \frac{\bar{P}_{srp}}{c} - \frac{\tilde{P}_{srp}}{c} \cos\left(\frac{2\pi d}{4017.75}\right) \tag{3.20}$$

where the mean $\bar{P}_{srp}$ and amplitude $\tilde{P}_{srp}$ are constants. d is the number of days since December 1^{st} of 2019, coinciding with the beginning of the current 25^{th} solar cycle, while c denotes the speed of light in vacuum.

In this context, Equation (3.20) could be linearly parameterized to account for the uncertain parameters in following integral concurrent learning formulation. However, better tracking and estimation performance is obtained when modeling the solar flux as a single unknown constant as the solar flux variation due to the Solar cycle is characterized by a low-frequency response. In addition, this results in less computational effort. It is part of future research to include the stochastic behaviour within the solar flux model to account for a more realistic case.

4 Lyapunov-Based Control Design

In this chapter, a Lyapunov-based control policy is derived in addition to an integral concurrent learning update law for online estimation of the irradiance from the Sun. Here, global exponential tracking of the estimated parameter and states of interest is proved for two sample missions: (1) a geostationary debris removal case and (2) an Earth-Mars interplanetary transfer orbit following a logarithmic spiral reference trajectory.

4.1 Geostationary Debris Removal Mission

For demonstration purposes, in the interest of increasing the semimajor axis by 377 km while keeping the eccentricity below 0.003 for a geostationary debris removal mission, we consider the semimajor axis a for active control as it is well known from the literature that only one orbital element can be controlled at a time [15]. We define a positive definite Lyapunov candidate function as

$$V(\Delta a, \Delta P_{srp}) \triangleq \frac{1}{2}\Delta a^2 + \frac{1}{2}\gamma^{-1}\Delta P_{srp}^2 > 0 \tag{4.1}$$

where $\Delta a \triangleq a - a_d$ and $\Delta P_{srp} \triangleq P_{srp} - \hat{P}_{srp}$ are the tracking and estimation errors, respectively. Here, a_d is the desired semimajor axis, while $\gamma \in \Re$ is a positive scalar constant control gain used to adjust the adaptation rate of the estimated parameter. By differentiating Equation (4.1), and substituting Equations (3.2a) and (3.16), we obtain the following expression after some algebraic manipulation.

$$\dot{V} = \frac{A_{tot}\cos(\phi_{inc})\hat{P}_{srp}\Delta a \boldsymbol{z}_a^T \tilde{\boldsymbol{u}}}{m} + \left(\frac{A_{tot}\cos(\phi_{inc})\Delta a \boldsymbol{z}_a^T \tilde{\boldsymbol{u}}}{m} - \frac{\dot{\hat{P}}_{srp}}{\gamma}\right)\Delta P_{srp} \tag{4.2}$$

where $\boldsymbol{z}_a^T$ is the GVE gradient of the orbital element of interest readily available from Equation (3.2a), and $\tilde{\boldsymbol{u}}$ is an auxiliary control variable defined as follows to facilitate readability and the subsequent control design.

$$\boldsymbol{z}_a^T = \frac{2}{n\sqrt{1-e^2}} \begin{bmatrix} e\sin(\upsilon) & \frac{p}{r} & 0 \end{bmatrix} \tag{4.3}$$

$$\tilde{\boldsymbol{u}} \triangleq b_1 \hat{\boldsymbol{e}}_{\odot} + (b_2 \cos(\phi_{inc}) + b_3)\hat{\boldsymbol{n}} \tag{4.4}$$

From Equation (4.2), the update law $\dot{\hat{P}}_{srp}$ is designed to remove the estimation error dependency as well as to guarantee global exponential tracking of the unknown SRP coefficient using an integral concurrent learning formulation suitable for the dynamics' structure.

$$\dot{\hat{P}}_{srp} \triangleq \frac{A_{tot}\cos(\phi_{inc})\gamma\Delta a \boldsymbol{z}_a^T \tilde{\boldsymbol{u}}}{m} + \gamma k_{ICL} \sum_{i=1}^{N} \mathcal{Y}_i \left[a(t_i) - a(t_i - \Delta t) - \mathcal{U}_i - \mathcal{Y}_i \hat{P}_{srp} \right] \tag{4.5}$$

where $k_{ICL} \in \Re$ is a positive scalar constant control gain and $N \in \mathbb{Z}^+$ is the number of input-output data pairs recorded. $\mathcal{U}_i = \mathcal{U}_i(t)$ and $\mathcal{Y}_i = \mathcal{Y}_i(t)$ are defined as

$$\mathcal{Y}_i(t) = \int_{t-\Delta t}^{t} \boldsymbol{z}_a^T(\boldsymbol{q}(\tau), \tau)\boldsymbol{y}(\tau)\,\mathrm{d}\tau \tag{4.6}$$

$$\mathcal{U}_i(t) = \int_{t-\Delta t}^{t} \boldsymbol{z}_a^T(\boldsymbol{q}(\tau), \tau)\boldsymbol{u}_d(\tau)\,\mathrm{d}\tau \tag{4.7}$$

where $\boldsymbol{y}(t)$ is the known SRP acceleration decoupled from the unknown solar flux while $\Delta t \in \Re$ is a positive constant denoting the integration time window. The concurrent learning term in Equation (4.5) represents saved data. $\mathcal{Y}_i(t)$ is the integral term that solely considers solar radiation pressure input while $\mathcal{U}_i(t)$ accounts for other orbital perturbations. For accurate solar flux estimation, high-precision algorithms of the most dominant gravitational perturbations as well as atmospheric drag are required when applicable.

$$\boldsymbol{y}(t) = \frac{VA_{tot}\cos\left(\phi_{inc}\right)}{m}\left(\frac{\mathrm{AU}}{r_{\odot}}\right)^{2}\left[b_1\hat{\boldsymbol{e}}_{\odot} + \left(b_2\cos\left(\phi_{inc}\right) + b_3\right)\hat{\boldsymbol{n}}\right] \tag{4.8}$$

For a detailed discussion on how to numerically integrate Equations (4.6) and (4.7) as well as on how to properly record data points for an optimal convergence rate, refer to References [11] and [12]. In short, sufficiently many different data pairs are required for accurate parameter estimation. One could define the minimum deviation between consecutive data pairs as a threshold to guarantee a diverse set. Alternatively, input-to-output data should be recorded to maximize the minimum eigenvalue of the summation as this value dictates the convergence rate of the estimates. However, this last method often adds more complexity and computational time based on storage capacity. In this sense, the update law in Equation (4.5) can be rewritten in an equivalent analysis form. This form of the update law suggests that if sufficiently rich input-to-output data are recorded, $\sum \mathcal{Y}_i^2$ will be positive definite.

$$\dot{\hat{P}}_{srp} = \frac{A_{tot}\cos\left(\phi_{inc}\right)\gamma\Delta a\boldsymbol{z}_a^T\tilde{\boldsymbol{u}}}{m} + \gamma k_{ICL}\sum_{i=1}^{N}\mathcal{Y}_i^2\Delta P_{srp} \tag{4.9}$$

To obtain this version of the update law, we integrate the spacecraft equation of motion that considers the time rate of change of the semimajor axis for the time window $[t-\Delta t, t]$.

$$\int_{t-\Delta t}^{t}\dot{a}(\tau)\,\mathrm{d}\tau = \int_{t-\Delta t}^{t}P_{srp}\boldsymbol{z}_a^T(\tau)\boldsymbol{y}(\tau)\,\mathrm{d}\tau + \int_{t-\Delta t}^{t}\boldsymbol{z}_a^T(\tau)\boldsymbol{u}_d(\tau)\,\mathrm{d}\tau \tag{4.10}$$

Consequently, we obtain the following relationship that relates the SRP coefficient to the measurable semimajor axis.

$$a(t) - a(t-\Delta t) = \mathcal{Y}(t)P_{srp} + \mathcal{U}(t) \tag{4.11}$$

In practice, one can estimate the semimajor axis given orbit determination algorithms that compute the spacecraft position and velocity vectors. Given this expression, we substitute $P_{srp} = \hat{P}_{srp} + \Delta P_{srp}$ as defined previously. If we assumed that the system is sufficiently excited over a finite duration of time $T \in \Re$ such that

$$\sum_{i=1}^{N} \mathcal{Y}_i^2 \geqslant \bar{\lambda} \quad \forall\, t \geqslant T \tag{4.12}$$

then global asymptotic tracking of the estimated parameters is guaranteed by Theorem 4.10 in the work of Khalil [32]. Here, $\bar{\lambda} \in \Re^+$ is an user-defined threshold. In this sense, $\dot{V}$ can be upper bounded as follows given the update law in Equation (4.9).

$$\dot{V} \leqslant \frac{A_{tot} \cos(\phi_{inc}) \hat{P}_{srp} \Delta a \boldsymbol{z}_a^T \tilde{\boldsymbol{u}}}{m} \tag{4.13}$$

Consequently, the following control law is designed for the sail's unit normal vector denoting the spacecraft attitude to guarantee a negative semi-definite Lyapunov function time derivative.

$$\hat{\boldsymbol{n}} = -\frac{m(\boldsymbol{z}_a^T \boldsymbol{z}_a)^{-1} \boldsymbol{z}_a k \Delta a}{\hat{P}_{srp} A_{tot}} \tag{4.14}$$

where $k \in \Re$ is a positive constant control gain designed to constrain the surface normal vector to be unitary. The term $b_1 \hat{\boldsymbol{e}}_\odot$ within the auxiliary control input $\tilde{\boldsymbol{u}}$ is neglected owing to the assumption of an ideal solar sail model. This is done to simplify the analysis and guarantee a feasible solution. With this choice of the control law given by Equation (4.14), by invoking Barbalat's Lemma while assuming bounded eccentricity, we can prove global asymptotic tracking of the semimajor axis a for any value of the reflectivity modulation ratio f.

$$\dot{V} \leqslant -k\cos^2(\phi_{inc})\Delta a^2 \leqslant 0 \quad \forall \quad \Delta a \neq 0 \tag{4.15}$$

Notice that the solar radiation pressure force exerted on the spacecraft acts in the opposite direction of the Sun. Thus, we restrict $\phi_{inc} \in [-\frac{\pi}{2}, \frac{\pi}{2}]$. As part of the control logic, when the required sail's orientation gives rise to an unattainable configuration, the sail's surface normal vector is aligned perpendicular to the Sun $\left(\phi_{inc} = \frac{\pi}{2}\right)$ such that the solar radiation pressure acceleration is zero. Additionally in this formulation, the control law for the reflectivity modulation ratio is adopted from Reference [8] to counteract the variation in the solar flux using RCDs. In short, the required sail's cone angle α and reflectivity modulation ratio are obtained using standard numerical schemes to match a desired reference trajectory assuming the clock angle δ equals its reference value. The same control scheme is used in the following Earth-Mars interplanetary transfer orbit considering a logarithmic spiral trajectory as the reference. The reference time-variant dimensionless acceleration along the transverse and radial directions in terms of $\bar{f}$, the reference reflectivity modulation ratio, and α^{ref}, the reference cone angle, are the following according to Caruso et al. [8].

$$\begin{aligned}\tilde{a}_r^{ref} = {} & \bar{f}b_1^{on}\cos(\alpha^{ref}) + (1-\bar{f})b_1^{off}\cos(\alpha^{ref}) \\ & +[\bar{f}b_2^{on} + (1-\bar{f})b_2^{off}]\cos^3(\alpha^{ref}) \\ & +[\bar{f}b_3^{on} + (1-\bar{f})b_3^{off}]\cos^2(\alpha^{ref})\end{aligned} \tag{4.16}$$

$$\tilde{a}_t^{ref} = \cos(\alpha^{ref})\sin(\alpha^{ref})\{[\bar{f}b_2^{on} + (1-\bar{f})b_2^{off}]\cos\alpha^{ref} + \bar{f}b_3^{on} + (1-\bar{f})b_3^{off}\} \tag{4.17}$$

Moreover, one can solve numerically for the required cone angle that would counteract the unknown solar flux component estimated by the ICL update law. For this, we solve Equation (4.18) using Newton's method.

$$
\begin{aligned}
&-K_6^2\cos^6(\alpha) + 2(K_1 - K_7)K_6\cos^5(\alpha) \\
&+\left[K_6^2 - (K_1 - K_7)^2 + 2K_2K_6 - K_4^2\right]\cos^4(\alpha) \\
&+\left[-2(K_1 - K_7)(K_2 + K_6) - 2K_4K_5\right]\cos^3(\alpha) \\
&+\left[-2K_2K_6 - K_2^2 - k_5^2 - 2K_3K_4\right]\cos^2(\alpha) \\
&+\left[2K_2(K_1 - K_7) - 2K_3K_5\right]\cos(\alpha) + (K_2^2 - K_3^2) = 0
\end{aligned}
\tag{4.18}
$$

Here, K_i, for $i = 1, ..., 7$, is defined as follows based on the dimensionless reference acceleration and the presumed value of the solar flux $\bar{W}$ during the preliminary phase of the mission. Moreover, W is the estimated solar flux at any given time t provided by the integral concurrent learning update law.

$$K_1 = \frac{\bar{W}}{W}\tilde{a}_r^{ref}(b_2^{on} - b_2^{off}) \tag{4.19a}$$

$$K_2 = \frac{\bar{W}}{W}\tilde{a}_r^{ref}(b_3^{on} - b_3^{off}) \tag{4.19b}$$

$$K_3 = \frac{\bar{W}}{W}\tilde{a}_t^{ref}(b_1^{on} - b_1^{off}) \tag{4.19c}$$

$$K_4 = \frac{\bar{W}}{W}\tilde{a}_t^{ref}(b_2^{on} - b_2^{off}) \tag{4.19d}$$

$$K_5 = \frac{\bar{W}}{W}\tilde{a}_t^{ref}(b_3^{on} - b_3^{off}) \tag{4.19e}$$

$$K_6 = b_1^{off}b_2^{on} - b_1^{on}b_2^{off} \tag{4.19f}$$

$$K_7 = b_1^{off} b_3^{on} - b_1^{on} b_3^{off} \tag{4.19g}$$

Ultimately, the reflectivity modulation ratio that provides the fraction of switched-on RCDs to account for solar flux fluctuations is given by

$$f = \frac{(\bar{W}/W)\tilde{a}_r^{ref} - (b_1^{off}\cos(\alpha) + b_2^{off}\cos^3(\alpha) + b_3^{off}\cos^2(\alpha))}{(b_1^{on} - b_1^{off})\cos(\alpha) + (b_2^{on} - b_2^{off})\cos^3(\alpha) + (b_3^{on} - b_3^{off})\cos^2(\alpha)} \tag{4.20}$$

4.2 Application to Earth-Mars Transfer Orbit

For an interplanetary Earth-Mars mission, consider a logarithmic spiral reference trajectory [3]. Here, the spacecraft attitude is fixed relative to the LVLH reference frame as the cone angle $\alpha \in [0, \pi/2]$ is constant and the clock angle is zero. The cone angle is defined as the angle between the surface normal vector and the in-track direction.

$$\hat{\boldsymbol{n}} = \begin{bmatrix} \cos(\alpha) & \sin(\alpha) & 0 \end{bmatrix}^T \tag{4.21}$$

In this sense, considering Equation (4.1) as a valid scalar positive definite Lyapunov candidate function and the update law given by Equation (4.5), analogously to the geostationary debris removal case, the Lyapunov function time derivative is upper bounded while estimation of the solar flux is guaranteed.

$$\dot{V} \leqslant \frac{A_{tot}\cos(\phi_{inc})\hat{P}_{srp}\Delta a \boldsymbol{z}_a^T \tilde{\boldsymbol{u}}}{m} \tag{4.22}$$

Here, Δa is a negative scalar value as the spacecraft is increasing its semimajor axis from a lower (Earth) to a higher orbit (Mars). The inner product $\boldsymbol{z}_a^T \tilde{\boldsymbol{u}}$ is expanded to point out the contribution of each term.

$$\begin{aligned} \boldsymbol{z}_a^T \tilde{\boldsymbol{u}} = & \frac{2e\sin(v)}{n\sqrt{1-e^2}}(b_1 + b_2\cos^2(\alpha) + b_3\cos(\alpha)) \\ & + \frac{2p}{nr\sqrt{1-e^2}}(b_2\cos(\alpha)\sin(\alpha) + b_3\sin(\alpha)) \end{aligned} \tag{4.23}$$

As the eccentricity is relatively small compared to the ratio of the orbit's semi-latus rectum to its radius, the first term in Equation (4.23) is neglected. As a result, the Lyapunov time derivative is proven to be negative definite throughout the entire interplanetary maneuver. As it is commonly done in the literature, the excess velocity is neglected and only the interplanetary arc is considered [3].

$$\dot{V} \leqslant -\frac{A_{tot}\cos(\phi_{inc}) \mid \Delta a \mid \boldsymbol{z}_a^T \hat{P}_{srp}}{m}\left[\frac{2p}{nr\sqrt{1-e^2}}(b_2\cos(\alpha)\sin(\alpha) + b_3\sin(\alpha))\right] \tag{4.24}$$

5 Numerical Simulations and Discussion

In this chapter, numerical simulations for two sample missions are considered to test the control formulation and estimation performance: (1) a geostationary debris removal case and (2) an Earth-Mars interplanetary transfer orbit following a logarithmic spiral reference trajectory. Results are compared to trajectories with no estimation to illustrate the need to account for solar flux fluctuations.

5.1 Geostationary Debris Removal Mission

For demonstration purposes, a Lyapunov-based adaptive control along with integral concurrent learning is simulated in *Matlab* for a geostationary solar sail spacecraft. It is desired to increase its semimajor axis by 377 km while keeping its eccentricity bellow 0.003. This is an example of a geostationary debris removal application using solar sails in accordance with the *IADC* Space Debris Mitigation Guidelines [41]. The solar sail to consider features a mass of 1050 kg and a total surface area of 800 m^2. It is assumed that 20% of the sail area has RCDs installed. The unknown solar flux was initialized to 1500 W/m^2. In reality, the true values of the solar flux time-varying model were adopted as $\bar{P}_{srp} = 1367$ W/m^2 and $\tilde{P}_{srp} = 0.6835$ W/m^2. The disturbing accelerations include the Earth's oblateness captured by the second zonal and tesseral harmonics in addition to solar and lunar gravity to simulate the gravitational effect of neighboring celestial bodies. The control gains were selected as $\gamma = 10^{-20}$ and $k_{ICL} = 10^{10}$, while $\bar{\lambda}$ was set to 1×10^{-3}. The reference trajectory given by Equation (4.14) was integrated simultaneously with the spacecraft's state vector. At each time step, the required cone angle and reflectivity modulation ratio was obtained using the current estimated solar flux giving a reference value of $P_{srp}^{ref} = 1375$ W/m^2. The algorithm adopted from Reference [8] was employed assuming a reference reflectivity modulation ratio of $\bar{f} = 0.9$. The same reference values were used for the interplanetary transfer orbit introduced in the next section.

The same adaptive control formulation discussed in this thesis was also considered for the eccentricity control of the spacecraft after the first phase of the maneuver was completed (*i.e.*, the semimajor axis control phase). As shown in Figures 5.1 and 5.3, the Lyapunov-based adaptive control law tracks the desired reference for both orbital elements one at a time within 220 days. Additionally, as a means to illustrate the benefit of estimating the solar flux using integral concurrent learning, results are compared to trajectories with no ICL estimation (*i.e.*, $k_{ICL} = 0$). As expected, as time progresses, the deviation of the trajectory without estimation becomes more predominant relative to its reference. For instance, Figure 5.2 and Figure 5.4 show the residual steady state error in the semimajor axis and eccentricity for all cases considered in this study, respectively. However, a more significant deviation from the reference trajectory is observed for the next case in which we consider an Earth-Mars transfer orbit.

Nevertheless, as illustrated in Figure 5.5, the estimated parameter converges to its true value in about 2 days to correctly model the time-varying solar flux model given by Equation (3.20). The residual steady state estimation error is recorded as 0.33 W/m^2. This clearly indicates that the proposed ICL formulation used to estimate the solar flux accurately approximates its actual value even for an uneducated initial guess as it is 1500 W/m^2. Moreover, over the full length of the mission, the mean estimation error is computed as 0.34 W/m^2 or equivalently 0.02%. It is important to note that better estimation was observed with smaller time steps within the simulation code to integrate the state vector. Figure 5.6 shows the constantly increasing behavior of $\sum \mathcal{Y}_i^2$ during the first phase of the maneuver. This indicates that the ICL terms given by Equations (4.6) and (4.7) integrate sufficiently rich data to accurately estimate the unknown solar flux.

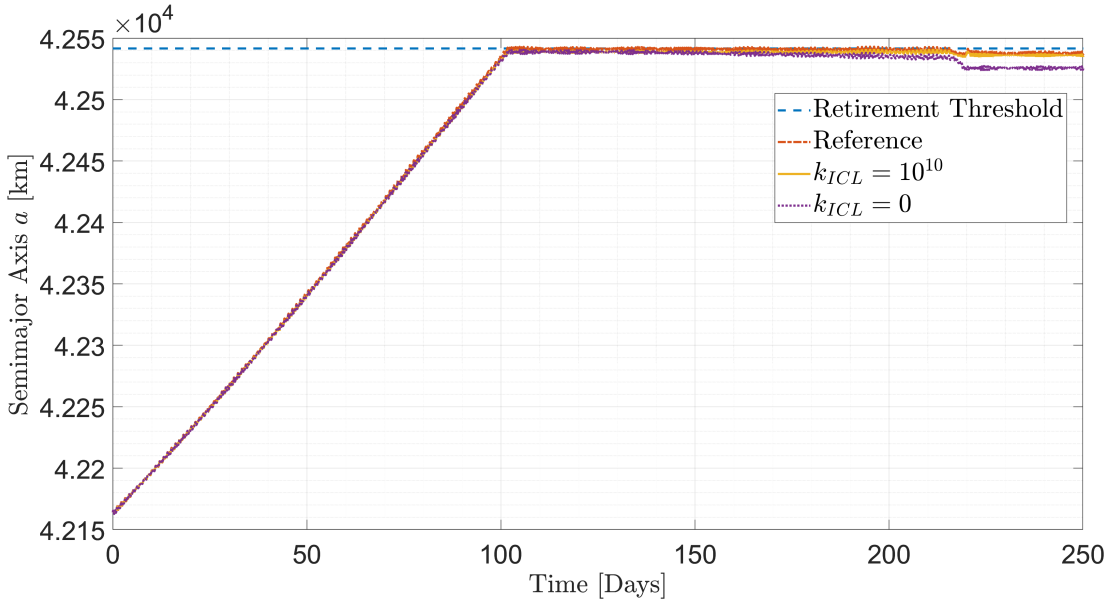

Figure 5.1 Semimajor axis for a GEO debris removal mission.

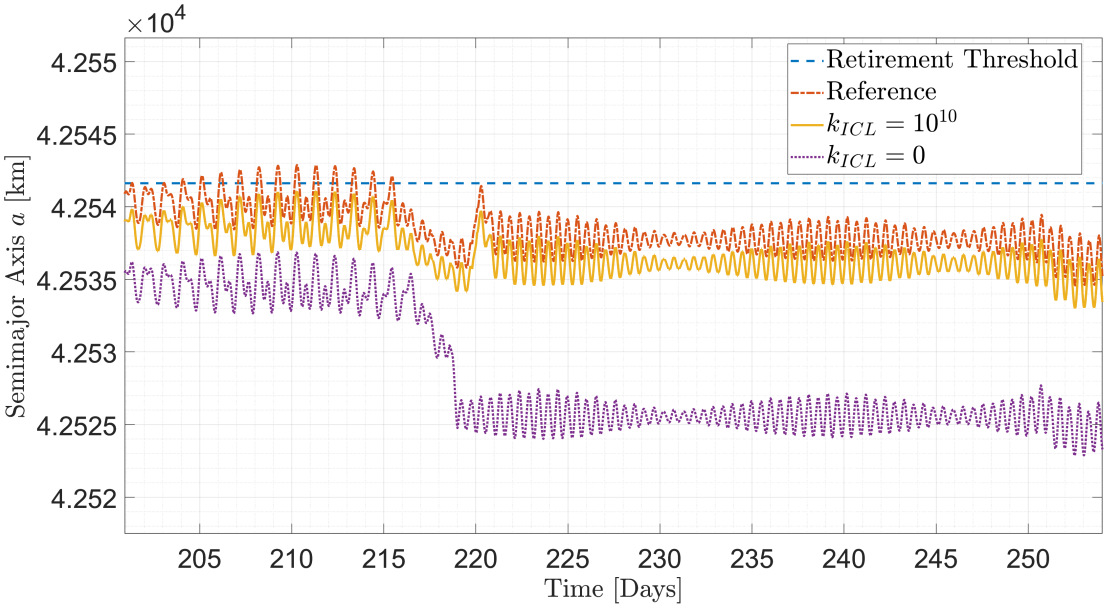

Figure 5.2 Semimajor axis steady state response for a GEO debris removal mission.

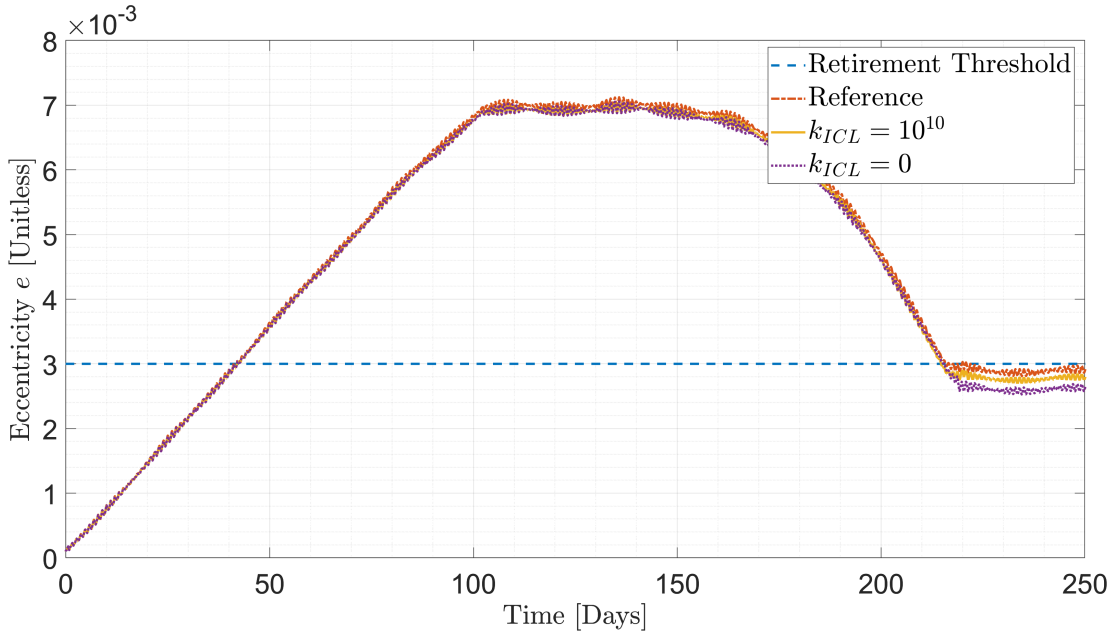

Figure 5.3 Eccentricity for a GEO debris removal mission.

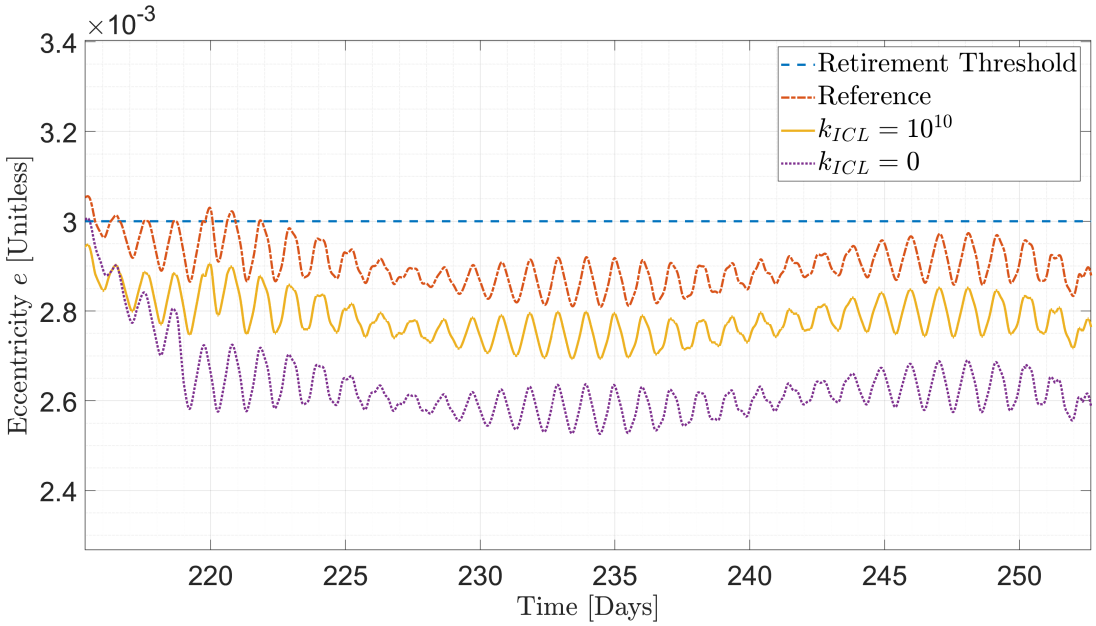

Figure 5.4 Eccentricity steady state response for a GEO debris removal mission.

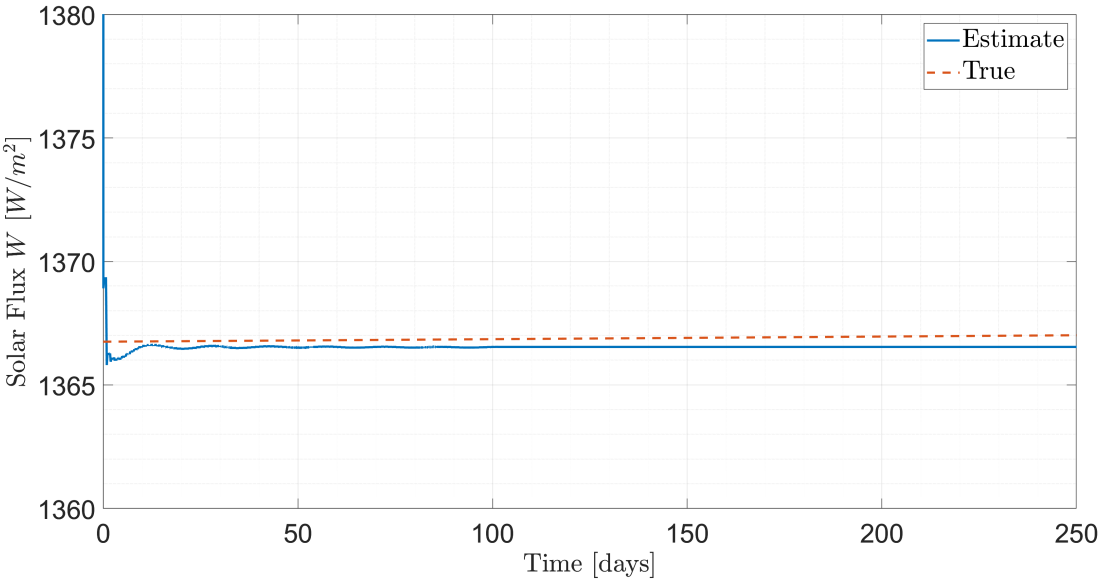

Figure 5.5 Solar flux estimation for GEO debris removal mission.

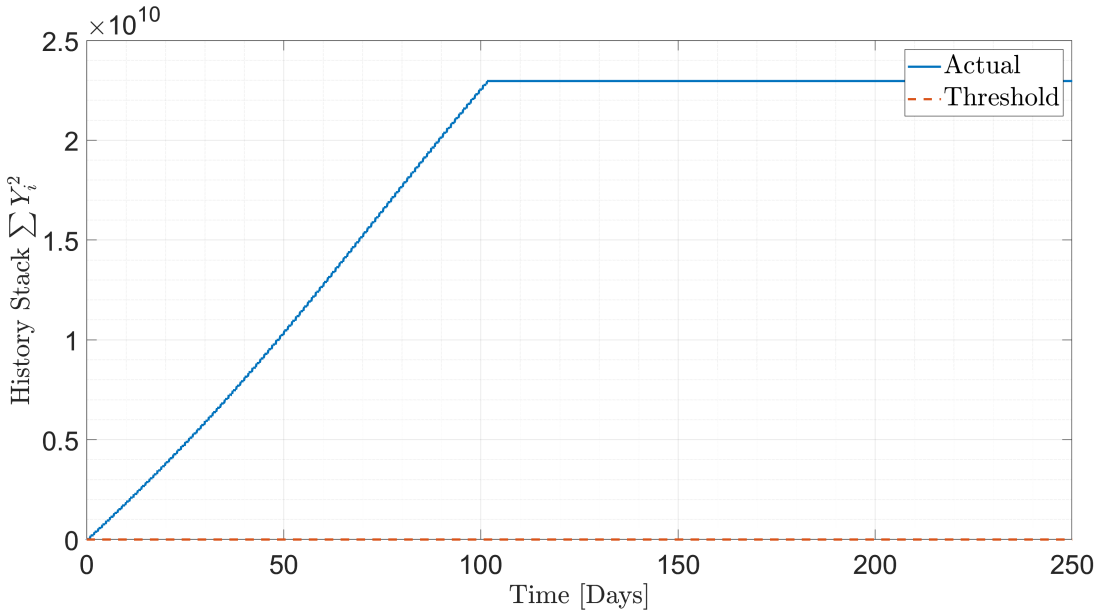

Figure 5.6 History stack of $\sum \mathcal{Y}_i^2$ for GEO debris removal mission.

5.2 Application to Earth-Mars Transfer Orbit

The proposed control system is tested with an additional application mission to better illustrate the need to account for the variation in the solar flux. The Lyapunov-based update law derived in this thesis is used to estimate the solar flux given a logarithmic spiral trajectory in which the reference cone angle is considered to be $\alpha_{ref} = 35.17^{\circ}$. This value of the cone angle was obtained following the optimal control problem in Reference [3] for an ideal solar sail to minimize flight time. An ephemeris-free interplanetary transfer orbit from Earth to Mars is illustrated as a means to show the benefit of estimating the solar flux. Here, the modified equinoctial orbital elements were used to describe the spacecraft state vector for numerical integration of the equations of motion. To avoid propagation of error within the simulation, the estimates' adaptation rate was set to zero after 73 days in simulation time. Similarly to the geostationary debris removal mission, the unknown solar flux was initialized to 1500 W/m^2. The true values of the solar flux time-varying model were simulated as $\bar{P}_{srp} =$ 1367 W/m^2 and $\tilde{P}_{srp} = 0.6835$ W/m^2. The control gains were selected as $\gamma = 10^{-40}$ and $k_{ICL} = 10^{20}$. It is assumed the solar sail features the same area-to-mass ratio as of the NEA Scout $A_{tot}/m = 6.07$ m^2/kg, and that 20% of the sail area has RCDs installed.

Figure 5.7 shows the logarithmic spiral trajectory with ICL estimation ($k_{ICL} = 10^{30}$) and with no adaptation ($k_{ICL} = 0$) compared to a reference. A closer view by Figure 5.8 points out the deviation of the trajectories considered in this study. This confirms that, given a wrong guess of the solar flux, the solar sail can significantly deviate from its reference. Figure 5.9 shows the ICL estimation of the unknown parameter. Here, the mean error is reported as 0.38 W/m^2, or equivalently 0.03%. The estimated solar flux converges to its true value within 15 days. The convergence criteria was set to 2 W/m^2.

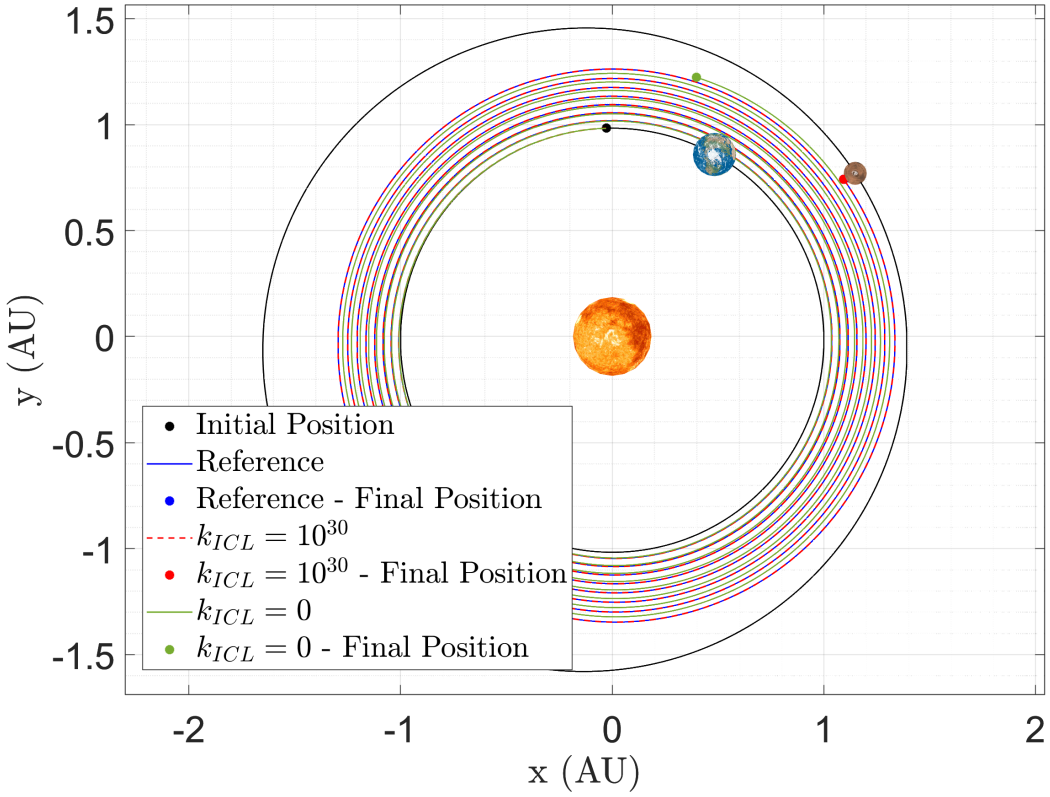

Figure 5.7 Earth-Mars transfer orbit.

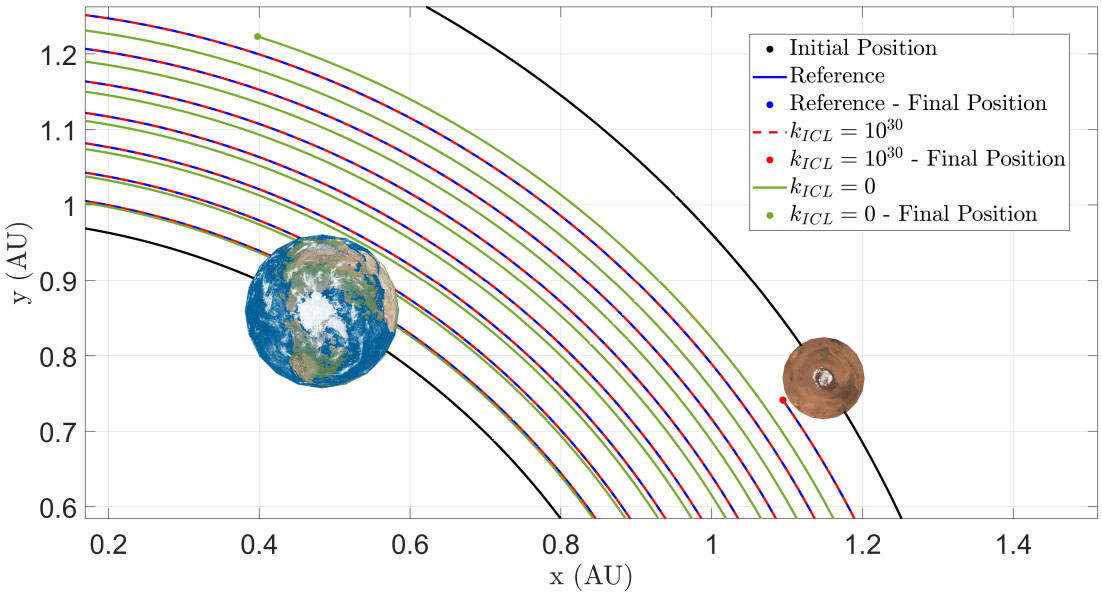

Figure 5.8 Earth-Mars transfer orbit at final target.

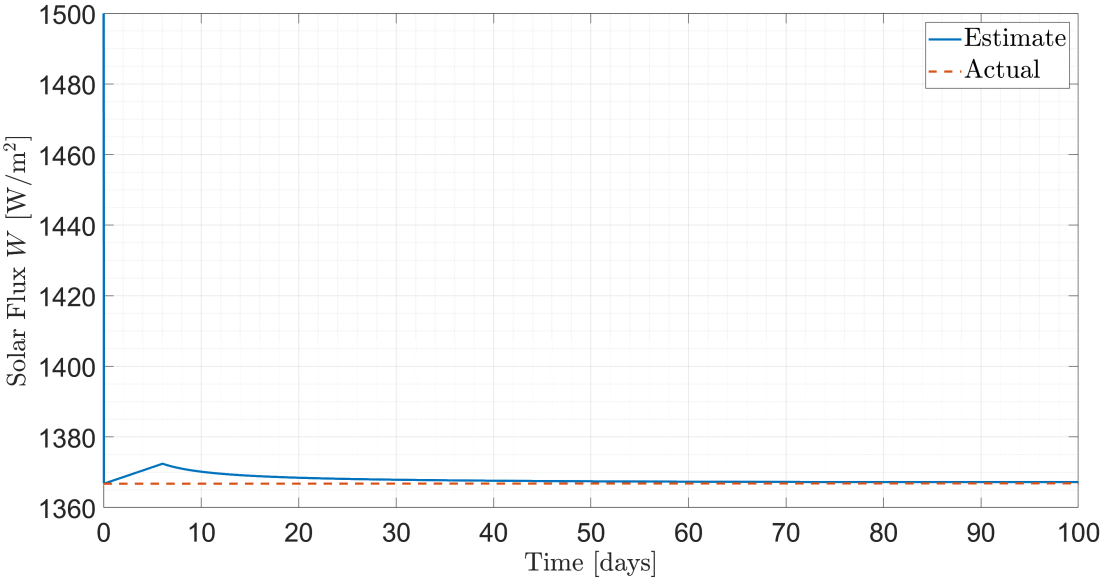

Figure 5.9 Solar flux estimation for Earth-Mars transfer orbit.

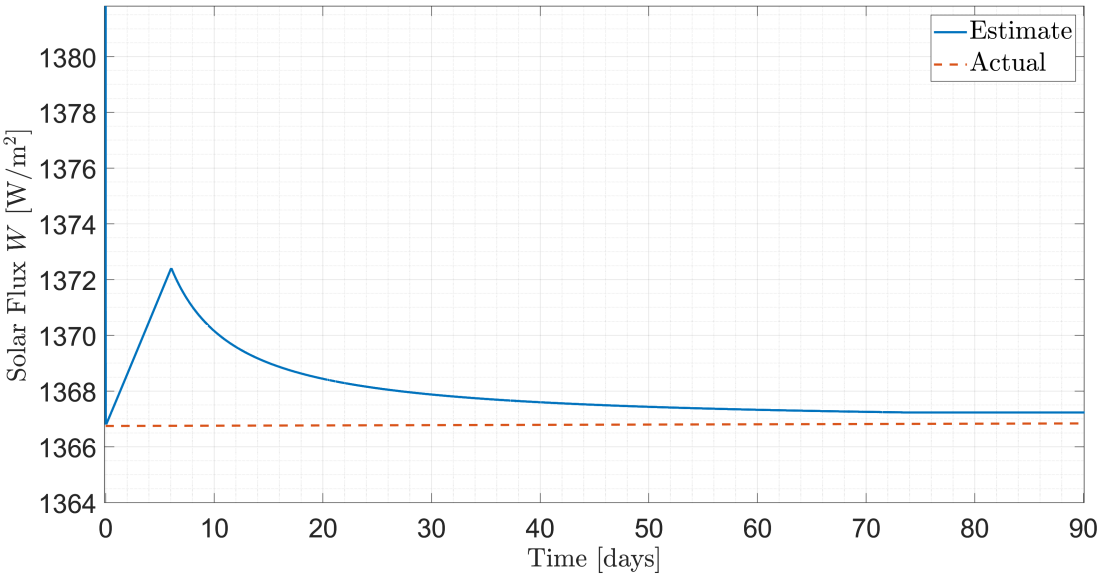

Figure 5.10 Close view solar flux estimation for Earth-Mars transfer orbit.

6 Conclusions and Future Work

Motivated by the desire to increase robustness and improve transient performance, the proposed adaptive control formulation demonstrates the benefit of estimating the solar flux using integral concurrent learning without satisfying the persistence of excitation condition. Results were compared to trajectories with no estimation to illustrate the need to account for solar flux fluctuations. Two missions were considered: (1) a geostationary debris removal case and (2) an Earth-Mars interplanetary transfer orbit following a logarithmic spiral reference trajectory. For near-Earth maneuvers, the steady state estimation error is recorded as 0.33 W/m^2. Similarly, the mean error for an Earth-Mars transfer is reported as 0.38 W/m^2, or equivalently 0.03%. This clearly indicates that the suggested adaptive control law used to estimate the solar flux accurately approximates its actual value.

Future research should include the stochastic solar flux behaviour within the estimation model. The potential to use integral concurrent learning for online estimation of unknown parameters is suggested for solar sailing formation flight maneuvers. Estimation of the thermo-optical film properties is also proposed and encouraged for future investigations. In this thesis, the stochastic solar flux variation was neglected as well as measurement noise in the orbital and attitude states of the solar sail. Additionally, the optical solar pressure model that captures the acceleration due to solar radiation pressure based on the thermo-optical film properties was assumed to be an exact representation of the spacecraft's dynamics. In this context, an extensive robustness to noise analysis is required to assess and test modifications to the control policy for future real-life applications in which one would need to estimate the solar flux to track a desired reference trajectory. This includes the implementation of robust adaptive control modifications such as the well-known sigma and e-modifications. As a means to account for a realistic evaluation through a high-fidelity simulation, future research should include radiometric tracking techniques for deep-space navigation to properly model in simulation measurement noise.

REFERENCES

[1] NASA, "Advanced Composite Solar Sail System: Using Sunlight to Power Deep Space Exploration," 2021. URL https://www.nasa.gov/directorates/spacetech/small_spacecraft/ACS3.

[2] Tsuda, Y., Mori, O., Funase, R., Sawada, H., Yamamoto, T., Saiki, T., Endo, T., Yonekura, K., Hoshino, H., and Kawaguchi, J., "Achievement of IKAROS-Japanese Deep Space Solar Sail Demonstration Mission," *Acta Astronautica*, Vol. 82, No. 2, 2013, pp. 183–188. https://doi.org/10.1016/j.actaastro.2012.03.032.

[3] Mclnnes, C. R., *Solar Sailing: Technology, Dynamics and Mission Applications*, 1^{st} ed., Springer-Verlag Berlin Heidelberg, New York, 1999.

[4] NASA, "NEA Scout," 2022. URL https://www.nasa.gov/content/nea-scout.

[5] NASA, "Diffractive Lightsails," 2019. URL https://www.nasa.gov/directorates/spacetech/niac/2019_Phase_I_Phase_II/Diffractive_Lightsails/.

[6] Niccolai, L., Mengali, G., Quarta, A. A., and Caruso, A., "Feedback Control Law of Solar Sail with Variable Surface Reflectivity at Sun-Earth Collinear Equilibrium Points," *Aerospace Science and Technology*, Vol. 106, No. 2, 2020, pp. 183–188. https://doi.org/10.1016/j.ast.2020.106144.

[7] Mu, J., Gong, S., and Li, J., "Reflectivity-Controlled Solar Sail Formation Flying for Magnetosphere Mission," *Aerospace Science and Technology*, Vol. 30, No. 1, 2013, pp. 339–348. https://doi.org/10.1016/j.ast.2013.09.002.

[8] Caruso, A., Mengali, G., Quarta, A. A., and Niccolai, L., "Solar Sail Optimal Control with Solar Irradiance Fluctuations," *Advances in Space Research*, Vol. 67, No. 9, 2021, pp. 2776–2783. https://doi.org/10.1016/j.asr.2020.05.037.

[9] Ceriotti, M., Harkness, P., and McRobb, M., "Variable-Geometry Solar Sailing: The Possibilities of the Quasi-Rhombic Pyramid," *Advances in Solar Sailing*, Springer, 2014, pp. 899–919. https://doi.org/10.1007/978-3-642-34907-2_54.

[10] Ishida, H., Chujo, T., Mori, O., and Kawaguchi, J., "Optimal Design of Advanced Reflectivity Control Device for Solar Sails Considering Polarization Properties of Liquid Crystal," *Proceedings of the 26th International Symposium on Space Flight Dynamics*, 2017. URL https://issfd.org/ISSFD_2017/paper/ISTS-2017-d-061__ISSFD-2017-061.pdf.

[11] Chowdhary, G., "Concurrent Learning for Convergence in Adaptive Control without Persistency of Excitation," Ph.D. thesis, Georgia Institute of Technology, 2010.

[12] Parikh, A., Kamalapurkar, R., and Dixon, W. E., "Integral Concurrent Learning: Adaptive Control with Parameter Convergence Using Finite Excitation," *International Journal of Adaptive Control and Signal Processing*, Vol. 33, No. 12, 2018, pp. 1775–1787. https://doi.org/10.1002/acs.2945.

[13] Vulpetti, G., "Effect of the Total Solar Irradiance Variations on Solar-Sail Low-Eccentricity Orbits," *Acta Astronautica*, Vol. 67, No. 1-2, 2010, pp. 279–283. https://doi.org/10.1016/j.actaastro.2010.02.004.

[14] Vulpetti, G., "Total Solar Irradiance Fluctuation Effects on Sailcraft-Mars Rendezvous," *Acta Astronautica*, Vol. 68, No. 5-6, 2011, pp. 644–650. https://doi.org/10.1016/j.actaastro.2010.01.010.

[15] Kelly, P., and Bevilacqua, R., "An Optimized Analytical Solution for Geostationary Debris Removal Using Solar Sails," *Acta Astronautica*, Vol. 162, No. 12, 2019, pp. 72–86. https://doi.org/10.1016/j.actaastro.2019.05.055.

[16] Carlesso, F., Barbosa, A. R., Antunes Vieira, L. E., Dal Lago, A., et al., "Solar Irradiance Variability Monitor for the Galileo Solar Space Telescope Mission: Con-

cept and Challenges," *Frontiers in Physics*, , No. 9, 2022, pp. 189–203. https://doi.org/10.3389/fphy.2022.869738.

[17] Harber, D., Castleman, Z., Drake, G., Van Dreser, S., Farber, N., Heuerman, K., Miller, M., Rutkowski, J., Sims, A., Sprunck, J., et al., "Compact Total Irradiance Monitor Flight Demonstration," *CubeSats and SmallSats for Remote Sensing III*, Vol. 11131, 2019, pp. 97–104. https://doi.org/10.1117/12.2531308.

[18] Funase, R., Shirasawa, Y., Mimasu, Y., Mori, O., Tsuda, Y., Saiki, T., and Kawaguchi, J., "On-Orbit Verification of Fuel-Free Attitude Control System for Spinning Solar Sail Utilizing Solar Radiation Pressure," *Advances in Space Research*, Vol. 48, No. 11, 2011, pp. 1740–1746. https://doi.org/10.1016/j.asr.2011.02.022.

[19] Gong, S., and Li, J., "Solar Sail Halo Orbit Control Using Reflectivity Control Devices," *Transactions of the Japan Society for Aeronautical and Space Sciences*, Vol. 57, No. 5, 2014, pp. 279–288. https://doi.org/10.2322/tjsass.57.279.

[20] Biggs, J. D., and Negri, A., "Orbit-Attitude Control in a Circular Restricted Three-Body Problem Using Distributed Reflectivity Devices," *Journal of Guidance, Control, and Dynamics*, Vol. 42, No. 12, 2019, pp. 2712–2721. https://doi.org/10.2514/1.G004493.

[21] Fröhlich, C., and Lean, J., "Solar Radiative Output and Its Variability: Evidence and Mechanisms," *The Astronomy and Astrophysics Review*, Vol. 12, No. 4, 2004, pp. 273–320. https://doi.org/10.1007/s00159-004-0024-1.

[22] Krivova, N. A., and Solanki, S. K., "Models of Solar Irradiance Variations: Current Status," *Journal of Astrophysics and Astronomy*, Vol. 29, 2008, pp. 151–158. https://doi.org/10.1007/s12036-008-0018-x.

[23] PMOD, and WRC, "Solar Constant: Construction of a Composite Total Solar Irradiance (TSI) Time-Series from 1978 to the Present," 2022. URL https://www.pmodwrc.ch/en/research-development/solar-physics/tsi-composite/.

[24] Vallado, D. A., *Fundamentals of Astrodynamics and Applications*, 4^{th} ed., Microcosm Press, Hawthorne, CA, 2013.

[25] NCAR, "Sunspot and Granulation," 1995. URL https://www2.hao.ucar.edu/education/pictorial/sunspot-and-granulation.

[26] Baird, C., "How Often Does The Sun's Magnetic Field Flip?" 2013. URL https://www.wtamu.edu/~cbaird/sq/2013/08/07/how-often-does-the-suns-magnetic-field-flip/.

[27] Sapritsky, V., and Prokhorov, A., *Absolute Primary Radiometric Thermometry*, Springer International Publishing, Cham, 2020. https://doi.org/10.1007/978-3-030-57789-6_9.

[28] Kopp, G., and Lawrence, G., "The Total Irradiance Monitor (TIM): Instrument Design," *Solar Physics*, Vol. 230, 2005, pp. 91–109. https://doi.org/10.1007/s11207-005-7446-4.

[29] Song, B., Ye, X., Finsterle, W., Gyo, M., Gander, M., Oliva, A. R., Pfiffner, D., Zhao, Y., and Fang, W., "The Fengyun-3E/Joint Total Solar Irradiance Absolute Radiometer: Instrument Design, Characterization, and Calibration," *Solar Physics*, Vol. 296, 2021. https://doi.org/10.1007/s11207-021-01794-5.

[30] Willson, R. C., "Active Cavity Radiometer Type IV," *Solar Physics*, Vol. 18, No. 2, 1979, pp. 179–188. https://doi.org/10.1007/BF00151387.

[31] Nguyen, N. T., *Model-Reference Adaptive Control*, Springer, 2018.

[32] Khalil, H., *Nonlinear Systems*, 3^{rd} ed., Prentice Hall, Upper Saddle River, NJ, 2002.

[33] Riano-Rios, C., Bevilacqua, R., and Dixon, W. E., "Differential Drag-Based Multiple Spacecraft Maneuvering and On-Line Parameter Estimation Using Integral Concurrent Learning," *Acta Astronautica*, Vol. 174, No. 9, 2020, pp. 189–203. https://doi.org/10.1016/j.actaastro.2020.04.059.

[34] Woodward, N., Sinclair, A., and Bevilacqua, R., "Online Estimation of Unknown Parameters of Highly Flexible Spacecraft Using Integral Concurrent Learning and Kane's Equation," *AAS Conference 23-144*, 2023.

[35] Curtis, H., *Orbital Mechanics for Engineering Students*, Butterworth-Heinemann, 2013.

[36] Walker, M. J., Ireland, B., and Owens, J., "A Set Modified Equinoctial Orbit Elements," *Celestial Mechanics*, Vol. 36, No. 4, 1985, pp. 409–419. https://doi.org/10.1007/BF01227493.

[37] Broucke, R. A., and Cefola, P. J., "On the Equinoctial Orbit Elements," *Celestial Mechanics*, Vol. 5, No. 3, 1972, pp. 303–310. https://doi.org/10.1007/BF01228432.

[38] Kechichian, J. A., "Equinoctial Orbit Elements: Application to Optimal Transfer Problems," *AIAA/AAS Astrodynamics Conference*, 1990, pp. 933–949. https://doi.org/10.2514/6.1990-2976.

[39] United States Naval Observatory, *The Astronomical Almanac*, US Government Printing Office, 2008.

[40] Heaton, A., Ahmad, N., and Miller, K., "Near Earth Asteroid Scout Thrust and Torque Model," *International Symposium on Solar Sailing*, 2017. URL https://ntrs.nasa.gov/citations/20170001502, paper no. M17-5721.

[41] Inter-Agency Space Debris Coordination Committee, "IADC Space Debris Mitigation Guidelines," 2020. URL https://orbitaldebris.jsc.nasa.gov/library/iadc-space-debris-guidelines-revision-2.pdf.

PUBLICATIONS

- **Luis Enrique Mendoza Zambrano** and Riccardo Bevilacqua, "Solar Sailing Adaptive Control Using Integral Concurrent Learning for Solar Flux Estimation", *American Astronautical Society Conference: Flight Space Mechanics Meeting*, Austin, TX, 2023, Paper No. AAS 23-146.

A Modified Equinoctial Orbital Elements

A.1 Position and Velocity Vectors

The spacecraft position and velocity vectors can be expressed in terms of the modified equinoctial orbital elements. In this way, the LVLH basis are conveniently obtained to construct the required transformation matrix Q.

$$\boldsymbol{r} = \begin{bmatrix} \frac{r}{s^2}[\cos(L) + \alpha^2 \cos(L) + 2hk \sin(L)] \\ \frac{r}{s^2}[\sin(L) - \alpha^2 \sin(L) + 2hk \cos(L)] \\ \frac{2}{s^2}[h \sin(L) - k \cos(L)] \end{bmatrix} \tag{A.1}$$

$$\boldsymbol{v} = \begin{bmatrix} -\frac{1}{s^2}\frac{\mu}{p}[\sin(L) + \alpha^2 \sin(L) - 2hk \cos(L) + g - 2fhk + \alpha^2 g] \\ -\frac{1}{s^2}\frac{\mu}{p}[-\cos(L) + \alpha^2 \cos(L) - 2hk \sin(L) - f + 2ghk + \alpha^2 f] \\ \frac{2}{s^2}\sqrt{\frac{\mu}{p}}[h \cos(L) + k \sin(L) + fh + gk] \end{bmatrix} \tag{A.2}$$

Here, α, s, and w are auxiliary variables used to facilitate readability. r is the spacecraft distance from the Earth.

$$r = \frac{p}{w} \tag{A.3}$$

$$\alpha^2 = h^2 - k^2 \tag{A.4}$$

$$s^2 = 1 + h^2 + k^2 \tag{A.5}$$

$$w = 1 + f \cos(L) + g \sin(L) \tag{A.6}$$

A.2 Classical Orbital Elements

The classical orbital elements required by the control and update policy are readily available given the modified equinoctial orbital elements as follows.

$$a = p/(1 - f^2 - g^2) \tag{A.7a}$$

$$e = \sqrt{f^2 + g^2} \tag{A.7b}$$

$$i = 2\tan^{-1}\left(\sqrt{h^2 + k^2}\right) \tag{A.7c}$$

$$\omega = \tan^{-1}\left(g/f\right) \tag{A.7d}$$

$$\Omega = \tan_2^{-1}\left(k, h\right) \tag{A.7e}$$

$$\theta = L - \tan^{-1}\left(g/f\right) \tag{A.7f}$$